Functional Radiogenetic Profiling Implicates ERCC6L2 in Non-homologous End Joining

Francica, Paola ; Mutlu, Merve ; Blomen, Vincent A ; Oliveira, Catarina ; Nowicka, Zuzanna ; Trenner, Anika ; Gerhards, Nora M ; Bouwman, Peter ; Stickel, Elmer ; Hekkelman, Maarten L ; Lingg, Lea ; Klebic, Ismar ; van de Ven, Marieke ; de Korte-Grimmerink, Renske ; Howald, Denise ; Jonkers, Jos ; Sartori, Alessandro A ; Fendler, Wojciech ; Chapman, J Ross ; Brummelkamp, Thijn ; Rottenberg, Sven

Abstract: Using genome-wide radiogenetic profiling, we functionally dissect vulnerabilities of cancer cells to ionizing radiation (IR). We identify ERCC6L2 as a major determinant of IR response, together with classical DNA damage response genes and members of the recently identified shieldin and CTC1-STN1-TEN1 (CST) complexes. We show that ERCC6L2 contributes to non-homologous end joining (NHEJ), and it may exert this function through interactions with SFPQ. In addition to causing radiosensitivity, ERCC6L2 loss restores DNA end resection and partially rescues homologous recombination (HR) in BRCA1-deficient cells. As a consequence, ERCC6L2 deficiency confers resistance to poly (ADP-ribose) polymerase (PARP) inhibition in tumors deficient for both BRCA1 and p53. Moreover, we show that ERCC6L2 mutations are found in human tumors and correlate with a better overall survival in patients treated with radiotherapy (RT); this finding suggests that ERCC6L2 is a predictive biomarker of RT response.

DOI: https://doi.org/10.1016/j.celrep.2020.108068

Cell Reports

Article

Functional Radiogenetic Profiling Implicates ERCC6L2 in Non-homologous End Joining

Graphical Abstract

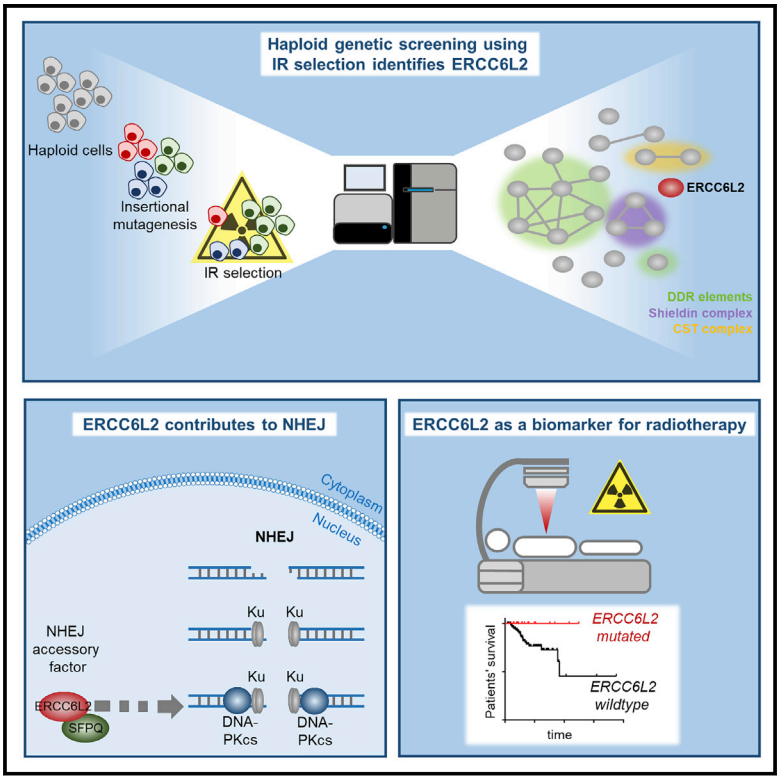

Highlights

- Radiogenetic profiling identifies *ERCC6L2* as a major determinant of IR response
- Loss of ERCC6L2 restores HR and causes PARPi resistance in BRCA1-deficient cells
- ERCC6L2 contributes to NHEJ, possibly through its interaction with SFPQ
- Patients with *ERCC6L2*-mutated UCEC show better survival upon RT

Authors

Paola Francica, Merve Mutlu, Vincent A. Blomen, ..., J. Ross Chapman, Thijn Brummelkamp, Sven Rottenberg

Correspondence

sven.rottenberg@vetsuisse.unibe.ch

In Brief

Francica et al. identify ERCC6L2 as an accessory NHEJ gene by using radiogenetic profiling in haploid cells. Loss of ERCC6L2 partially restores HR in BRCA1-deficient cells, and ERCC6L2 may be a useful predictive biomarker of radiotherapy response.

Francica et al., 2020, Cell Reports *32*, 108068
August 25, 2020
https://doi.org/10.1016/j.celrep.2020.108068

CellPress

Cell Reports

CellPress
OPEN ACCESS

Article

Functional Radiogenetic Profiling Implicates ERCC6L2 in Non-homologous End Joining

Paola Francica,[1,11] Merve Mutlu,[1,11] Vincent A. Blomen,[2,3] Catarina Oliveira,[4] Zuzanna Nowicka,[5] Anika Trenner,[6] Nora M. Gerhards,[1] Peter Bouwman,[3,7] Elmer Stickel,[2,3] Maarten L. Hekkelman,[2,3] Lea Lingg,[1] Ismar Klebic,[1] Marieke van de Ven,[8] Renske de Korte-Grimmerink,[8] Denise Howald,[1] Jos Jonkers,[3,7] Alessandro A. Sartori,[6] Wojciech Fendler,[5,9] J. Ross Chapman,[4] Thijn Brummelkamp,[2,3] and Sven Rottenberg[1,7,10,12,*]

[1]Institute of Animal Pathology, Vetsuisse Faculty, University of Bern, 3012 Bern, Switzerland
[2]Division of Biochemistry, the Netherlands Cancer Institute, 1066CX Amsterdam, the Netherlands
[3]Oncode Institute, the Netherlands Cancer Institute, 1066CX Amsterdam, the Netherlands
[4]Medical Research Council (MRC) Molecular Haematology Unit, Weatherall Institute of Molecular Medicine, University of Oxford, Oxford OX3 9DS, UK
[5]Department of Biostatistics and Translational Medicine, Medical University of Lodz, 92-215 Lodz, Poland
[6]Institute of Molecular Cancer Research, University of Zurich, 8057 Zurich, Switzerland
[7]Division of Molecular Pathology, the Netherlands Cancer Institute, 1066CX Amsterdam, the Netherlands
[8]Mouse Clinic for Cancer and Aging Research (MCCA), Preclinical Intervention Unit, the Netherlands Cancer Institute, 1066CX Amsterdam, the Netherlands
[9]Department of Radiation Oncology, Dana-Farber Cancer Institute, Boston, MA 02215, USA
[10]Bern Center for Precision Medicine, University of Bern, 3012 Bern, Switzerland
[11]These authors contributed equally
[12]Lead Contact
*Correspondence: sven.rottenberg@vetsuisse.unibe.ch
https://doi.org/10.1016/j.celrep.2020.108068

SUMMARY

Using genome-wide radiogenetic profiling, we functionally dissect vulnerabilities of cancer cells to ionizing radiation (IR). We identify ERCC6L2 as a major determinant of IR response, together with classical DNA damage response genes and members of the recently identified shieldin and CTC1-STN1-TEN1 (CST) complexes. We show that ERCC6L2 contributes to non-homologous end joining (NHEJ), and it may exert this function through interactions with SFPQ. In addition to causing radiosensitivity, ERCC6L2 loss restores DNA end resection and partially rescues homologous recombination (HR) in BRCA1-deficient cells. As a consequence, ERCC6L2 deficiency confers resistance to poly (ADP-ribose) polymerase (PARP) inhibition in tumors deficient for both BRCA1 and p53. Moreover, we show that ERCC6L2 mutations are found in human tumors and correlate with a better overall survival in patients treated with radiotherapy (RT); this finding suggests that ERCC6L2 is a predictive biomarker of RT response.

INTRODUCTION

Radiotherapy (RT) is one of the most commonly used anti-cancer therapies in the clinic. About 50% of all cancer patients will receive RT alone or in combination with chemotherapy as part of their treatment regimen (Barton et al., 2014; Delaney et al., 2005). Despite the major benefits of RT, local therapy resistance together with the development of early and late RT-related side effects remain major obstacles for its success.

RT results in DNA double-strand breaks (DSBs), which are highly toxic to cells (Ciccia and Elledge, 2010; Jackson and Bartek, 2009; Setiaputra and Durocher, 2019). The repair of DSBs relies predominantly on two major pathways: non-homologous end joining (NHEJ) and homologous recombination (HR) (Schimmel et al., 2019). Because the cytotoxic effect of RT relies on the generation of DNA damage, differences in the DNA damage response (DDR) can directly affect a tumor's response to RT. Most cancers have lost a critical DDR pathway during tumor evolution (Lord and Ashworth, 2012; Nickoloff et al., 2017); thus, many patients respond to clinical interventions that cause DNA damage, including RT and chemotherapy, by using DNA crosslinkers. Such regimens exploit DNA repair defects intrinsic to tumors to selectively eliminate cancer cells, whereas normal cells with an intact DDR can still cope. These DNA repair defects include mutations of core NHEJ factors, such as Ku70, XRCC4, LIG4, XLF, DCLRE1C, or PRKDC, which have been shown to cause radiosensitivity in various tumor models and in patients (Sishc and Davis, 2017; Trenner and Sartori, 2019). The identification of new vulnerabilities in the DDR of cancer cells is therefore crucial for the future development of treatment strategies that specifically sensitize tumors to RT.

One approach to identify such vulnerabilities is by screening for genetic mutations that selectively sensitize cells to a

treatment (Gerhards and Rottenberg, 2018). Recently, genome-wide insertional mutagenesis screens in haploid cells have identified unknown genetic vulnerabilities to microtubule-targeting drugs (Gerhards et al., 2018). With a related technique, new mechanisms of platinum drug or topoisomerase inhibitor resistance were similarly discovered (Planells-Cases et al., 2015; Wijdeven et al., 2015). Furthermore, library-based genome-wide screens have significantly advanced our understanding of the mechanisms in which cancer cells are sensitized to, and become resistant to, clinically relevant inhibitors of the poly (ADP-ribose) polymerase enzymes (PARPi) (Barazas et al., 2018; Gogola et al., 2018; Noordermeer et al., 2018; Tkáč et al., 2016; Xu et al., 2015). This approach has led to the identification of the precise DSB repair proteins responsible for the efficacy of PARPi in selectively killing BRCA1-deficient cancer cells, including 53BP1 (Bouwman et al., 2010), REV7/MAD2L2 (Xu et al., 2015), SHLD1-3 (Noordermeer et al., 2018), HELB (Tkáč et al., 2016), the CTC1-STN1-TEN1 (CST) complex (Barazas et al., 2018), DYNLL1 (He et al., 2018), and PARG (Gogola et al., 2018).

Here, we report the implementation of a genome-wide functional screen to discover genes that are involved in the cellular response to fractionated ionizing radiation (IR). In validation of this approach, in which we utilized saturating retrovirus-mediated insertional mutagenesis to screen for IR-modulating genes in the human haploid cell line HAP1, we identified a multitude of genes encoding well-established DSB repair factors. Indeed, Ataxia telangiectasia mutated (ATM), DNA-dependent protein kinase catalytic subunit (DNA-PKcs), Artemis (DCLRE1C), and RAD51B, proteins already known to be essential for cellular survival following IR, were among our highest ranking hits. Besides these proteins, our screen was enriched for additional genes that have been poorly characterized in terms of their contribution to IR responses and the cellular response to DSBs. One such gene encoded the SNF2 family helicase protein ERCC6L2, a protein whose deficiency was recently linked to an inherited human syndrome characterized by late-onset bone marrow failure and developmental abnormalities that included microcephaly (Bluteau et al., 2018; Järviaho et al., 2018; Shabanova et al., 2018; Tummala et al., 2014; Zhang et al., 2016). In addition, a homozygous *ERCC6L2* mutation has been implicated in acute myeloid leukemia (Douglas et al., 2019). Here, we reveal ERCC6L2 to be an important mediator of the cellular response to RT, an effect we link to its likely participation in NHEJ-dependent DSB repair. We furthermore find that ERCC6L2 deficiency confers significant PARPi resistance to murine BRCA1-deficient tumor cells, an effect reminiscent of proteins linked to the 53BP1 pathway-dependent resection inhibition during NHEJ. Consistent with this finding, we reveal that ERCC6L2 inhibits DNA end resection and show it to be important for immunoglobulin class-switch recombination in murine B cells. Altogether, our work reveals a previously unappreciated function for ERCC6L2 in NHEJ, a role that contributes to cellular response to RT-induced DNA damage and also the therapeutic response of BRCA1-deficient cells to clinical PARPi. Given that ERCC6L2 is frequently mutated in human cancer, our data also suggest that ERCC6L2 may be a useful biomarker to predict RT responses.

RESULTS

Genome-wide Loss-of-Function Screens Identify Genes That Increase IR Sensitivity

To functionally dissect the genes that may be dispensable for the growth of cells under standard culture conditions but become essential for cell fitness following IR exposure, we carried out a genome-wide loss-of-function screen in human haploid cells. Similar to a previous study in which we identified genes that affect the action of microtubule-targeting drugs (Gerhards et al., 2018), we applied an IR selection that causes moderate fitness reduction in HAP1 cells. After gene-trap mutagenesis, 10^8 HAP1 cells were seeded and irradiated over the next 3 consecutive days with daily doses of 1.5 Gy. Cells were fixed on day 10 and then sorted for 1n DNA content before amplification of gene-trap insertion sites and deep sequencing (Figure 1A). The reads were aligned to the human genome, and all independent gene-trap insertion sites and their orientation in relation to the transcriptional direction of individual genes were quantified in the IR-selected datasets. The gene-trap is designed to only disrupt the gene upon integration in a sense orientation, and hence, the proportion of sense integrations can be utilized as a measure of gene essentiality. Next, the ratio of gene-trap sense insertions to antisense integrations was determined for each gene. Candidate genes that significantly affect radiosensitivity were identified by comparing IR-selected datasets to four independent wild-type (WT) control datasets (Blomen et al., 2015; Tables S1 and S2). The significance of the hits comprise both enrichment and depletion of sense insertions compared to the unselected conditions. However, most of the candidates passing our stringent filtering criteria were depleted in their sense integrations after IR selection (Figures 1B and 1C). This finding indicates that these candidate genes are essential for fitness under IR selection.

A combined analysis of two replicate screens revealed 21 genes that become essential for cell fitness under IR selection (Figure 1D; Table S3). A total of 15 out of the 21 genes belong to the Gene Ontology term "DNA metabolism" and 12/21 to the biologic function of "DNA repair." Among these genes, some are well-known DNA repair factors involved in NHEJ or HR, including those already well studied in the context of cellular responses to irradiation (e.g. *ATM*, *PRKDC/DNA-PKcs*, *DCLRE1C/Artemis*, *RAD51B*, and *RNF168*).

The enrichment of these factors served as a validation of our screens, also re-confirming the relevance of these DNA repair pathways in providing fitness to cells exposed to IR (Figure 1E). Importantly, our screen also identified several candidate genes not previously implicated in IR survival response, nor linked to any particular DSB repair pathway.

Loss of *Ercc6l2* Induces IR Sensitivity and PARPi Resistance in BRCA1;p53-Deficient Cells

Among the significant hits from our haploid genetic screen, *ERCC6L2* (Figures S1A and S1B), a gene mutated in a hereditary bone marrow failure syndrome (Bluteau et al., 2018; Järviaho

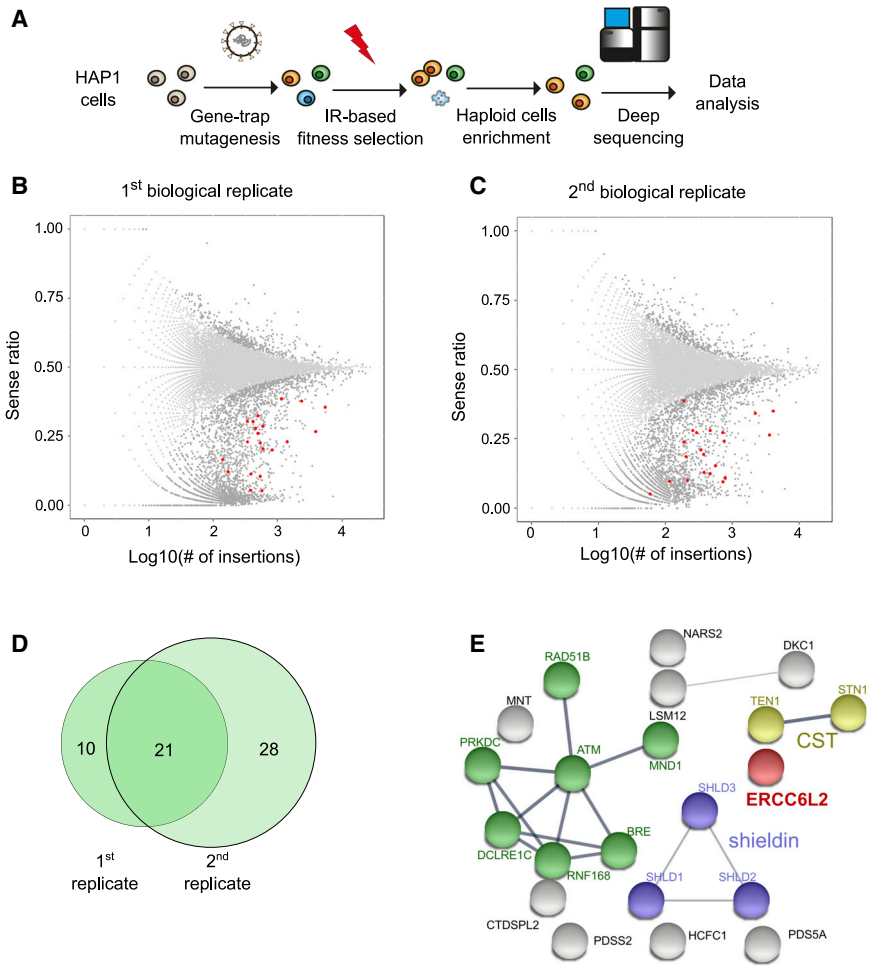

Figure 1. Genome-wide Loss-of-Function Screens Identify Genes That Increase IR Sensitivity

(A) Outline of the haploid genetic screening setup.

(B and C) Sense integration to total number of insertions plotted as fish tail plots from two individual biological replicates of irradiation (IR)-selected haploid genetic screens. Significantly altered genes are shown in dark gray, and genes significantly influencing the response to IR in both biological replicates are shown in red.

(D) Venn scheme comparing the hits from each biological replicate.

(E) STRING interaction map of the 21 significant hits that came up from both biological replicates.

See also Figure S1, Table S1, S2, and S3.

et al., 2018; Shabanova et al., 2018; Tummala et al., 2014; Zhang et al., 2016), caught our attention, as little is known about its function in DSB repair (Figure 1E).

To test whether depletion of ERCC6L2 causes radiosensitivity in the context of cell lines proficient or deficient for HR, we used lentiviral CRISPR-Cas9 gene targeting constructs to generate polyclonal knockout cell lines for *Ercc6l2* in the BRCA1-deficient KB1P-G3 and BRCA1-proficient KB1P-G3B1+ cell lines derived from our genetically engineered mouse model (GEMM) for *Brca1*-mutated breast cancer (*K14cre;Brca1*$^{F/,F}$*p53*$^{F/F}$). The KB1P-G3 cell line lacks BRCA1-dependent HR-directed DNA repair due to an irreversible *Brca1* deletion (Jaspers et al., 2013) and KB1P-G3B1+ cells have intact HR due to reintroduction of the full-length human *BRCA1* coding sequence (Barazas et al., 2019). Both lines were then examined for irradiation sensitivity to investigate whether the phenotype observed upon loss of *Ercc6l2* synergized with loss of the HR pathway.

Using tracking of indels by decomposition (TIDE) analysis (Brinkman et al., 2014), we confirmed efficient modification of the target sites in the polyclonal population (Figures S2A and S2B). *Ercc6l2*-depleted cells were subsequently exposed to IR *in vitro* (3 doses of 2, 3 or 4Gy for KB1P-G3 or 4, 5 or 6Gy for KB1P-G3B1+ cells), and both their growth and clonogenic capacity were compared with that of cells transduced with non-targeting (NT) single guide RNAs (sgRNAs). These experiments revealed that *Ercc6l2* loss resulted in increased sensitivity to IR in both BRCA1-deficient and -proficient cells (Figures 2A, S2C, S2F, S2G, and S2N). Moreover, monoclonal knockout lines derived from KB1P-G3B1+ polyclonal cells showed increased IR sensitivity (Figures S2D and S2E). Using TIDE analysis, we also demonstrated a selection against frameshift-mutated alleles in favor of the WT *Ercc6l2* alleles upon IR in both BRCA1-reconstituted and -deficient cells (Figures 2B and S2H). This finding confirms that the loss of *Ercc6l2* sensitizes cells to IR irrespective of BRCA1 status, confirming that the DNA repair defects that accompany ERCC6L2 loss synergize with HR deficiency (HRD) and implicating ERCC6L2 in a distinct DNA repair pathway. To exclude off-target effects, *Ercc6l2*-deleted cells were complemented with *Ercc6l2* cDNA (Figures 2E and 2G). Indeed, ERCC6L2 complementation rescued IR sensitivity, in contrast to cells transduced with the empty-vector control (Figure 2F). To understand which structural domains in ERCC6L2 were important for mediating response to IR, we also complemented ERCC6L2-depleted cells with mutant forms of the gene. Mutations of a conserved sequence within the Hebo domain (*Ercc6l2*$^{\Delta Hebo}$; see Method Details) rescued ERCC6L2 function, whereas mutations of the SNF2/ATPase domain (*Ercc6l2*$^{\Delta SNF2}$; see Method Details) at the N-terminus of the protein failed to do so (Figure 2F). These data show that the SNF2/ATPase protein domain is mandatory for ERCC6L2 function.

Besides genes encoding classical DNA repair factors, we notably detected genes encoding three subunits of the recently discovered Shieldin complex (*SHLD1/C20orf196*, *SHLD2/FAM35A*, and *SHLD3* [included in the *TRAPPC13* gene]) (Noordermeer et al., 2018; Ghezraoui et al., 2018) enriched in our screens. Members of the trimeric CST complex, *STN1* (also called OBFC1), *TEN1*, and *CTC1* (significant hit in the 2nd replicate; Table S2), were similarly enriched, collectively confirming the importance of 53BP1-pathway-dependent NHEJ, which

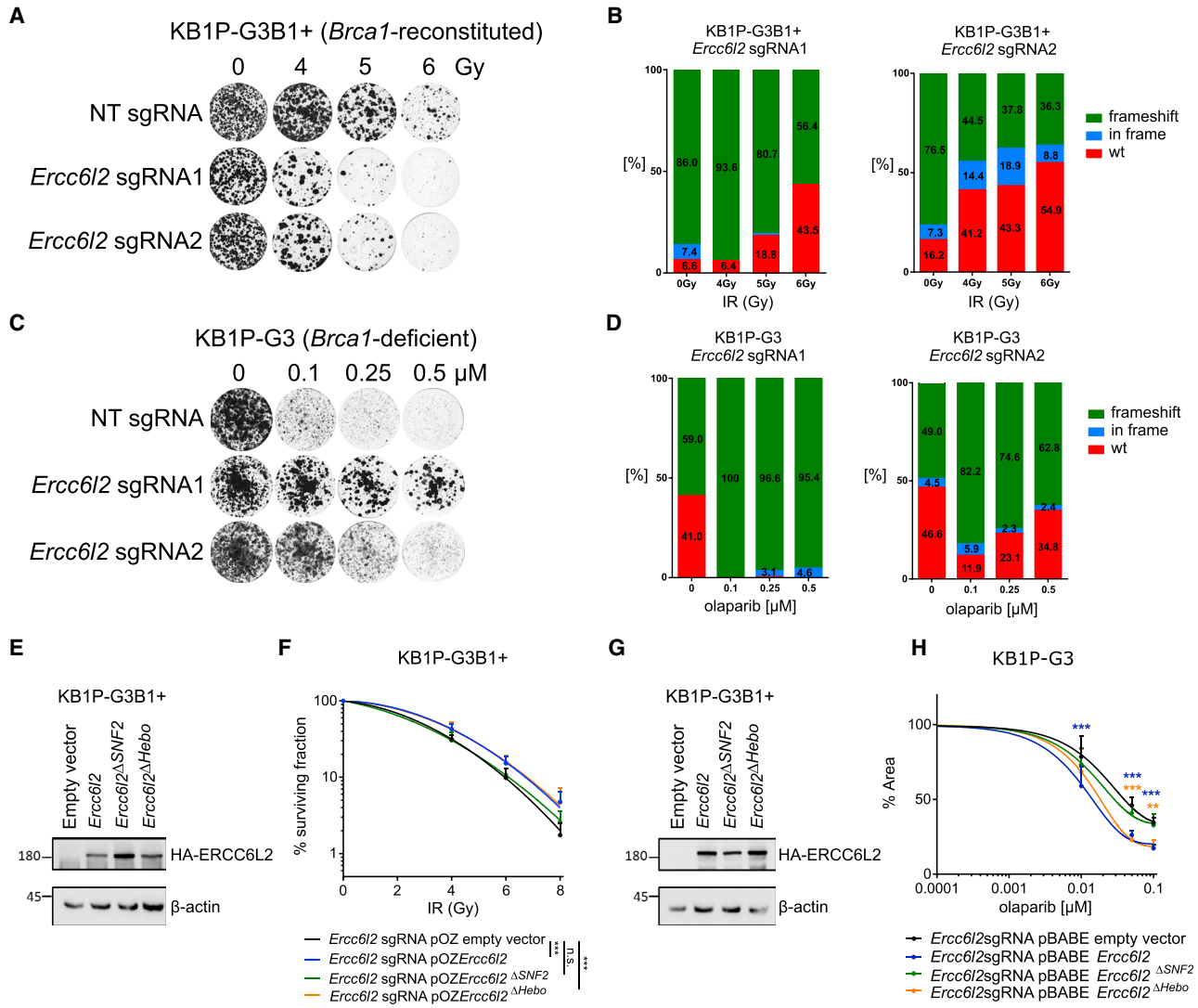

Figure 2. Loss of *Ercc6l2* Induces IR Sensitivity and PARPi Resistance in BRCA1;p53-Deficient Cells

(A) Growth assay of BRCA1-proficient KB1P-G3B1+ cells modified by CRISPR-Cas9 with the indicated sgRNAs following IR treatment.

(B) TIDE analysis showing the shift in allelic modification frequencies upon IR of *Ercc6l2*-mutated KB1P-G3B1+ cells.

(C) Growth assay in the presence of olaparib selection of BRCA1-deficient KB1P-G3 cells modified by CRISPR-Cas9 with the indicated sgRNAs.

(D) TIDE analysis showing the shift in allelic modification frequencies upon olaparib selection of *Ercc6l2*-mutated KB1P-G3 cells.

(E) Western blotting showing the hemagglutinin (HA)-ERCC6L2 levels of *Ercc6l2* WT, *Ercc6l2*$^{\Delta Hebo}$, and *Ercc6l2*$^{\Delta SNF2}$ constructs that were complemented in *Ercc6l2*-mutated KB1P-G3B1+ cells. β-actin was used as a loading control.

(F) Clonogenic survival of irradiated ERCC6L2-deficient KB1P-G3B1+ cells that were rescued with the indicated cDNA constructs. Data represent mean ± SD of three independent repeats. Statistics were calculated using CFAssay in R. ***$p < 0.001$.

(G) Western blotting showing the HA-ERCC6L2 levels of *Ercc6l2* WT, *Ercc6l2*$^{\Delta Hebo}$, and *Ercc6l2*$^{\Delta SNF2}$ constructs that were complemented in *Ercc6l2*-mutated KB1P-G3 cells.

(H) Growth assay in the presence of olaparib selection with *Ercc6l2*-knockout KB1P-G3 cells that were rescued with the indicated cDNA constructs. Data represent mean ± SD of three independent repeats and were fitted to a four parameter logistic (4PL) sigmodial curve. Statistical analysis was performed using 2-way ANOVA followed by Dunnett's test. *$p < 0.05$, **$p < 0.01$, ***$p < 0.001$.

See also Figure S2.

depends on shieldin and CST complexes, in the cellular response to RT. The 53BP1 pathway genes are known to cause intermediate radiosensitivity when depleted; yet, their deletion in BRCA1-deficient cells leads to a restoration of HR and near-complete resistance to PARPi (Barazas et al., 2018; Dev et al., 2018; Findlay et al., 2018; Gao et al., 2018; Ghezraoui et al., 2018; Gupta et al., 2018; Mirman et al., 2018; Noordermeer et al., 2018; Tomida et al., 2018). Given that ERCC6L2 co-enriched with these genes in our screen, we surmised that ERCC6L2 might similarly function in the 53BP1 pathway and

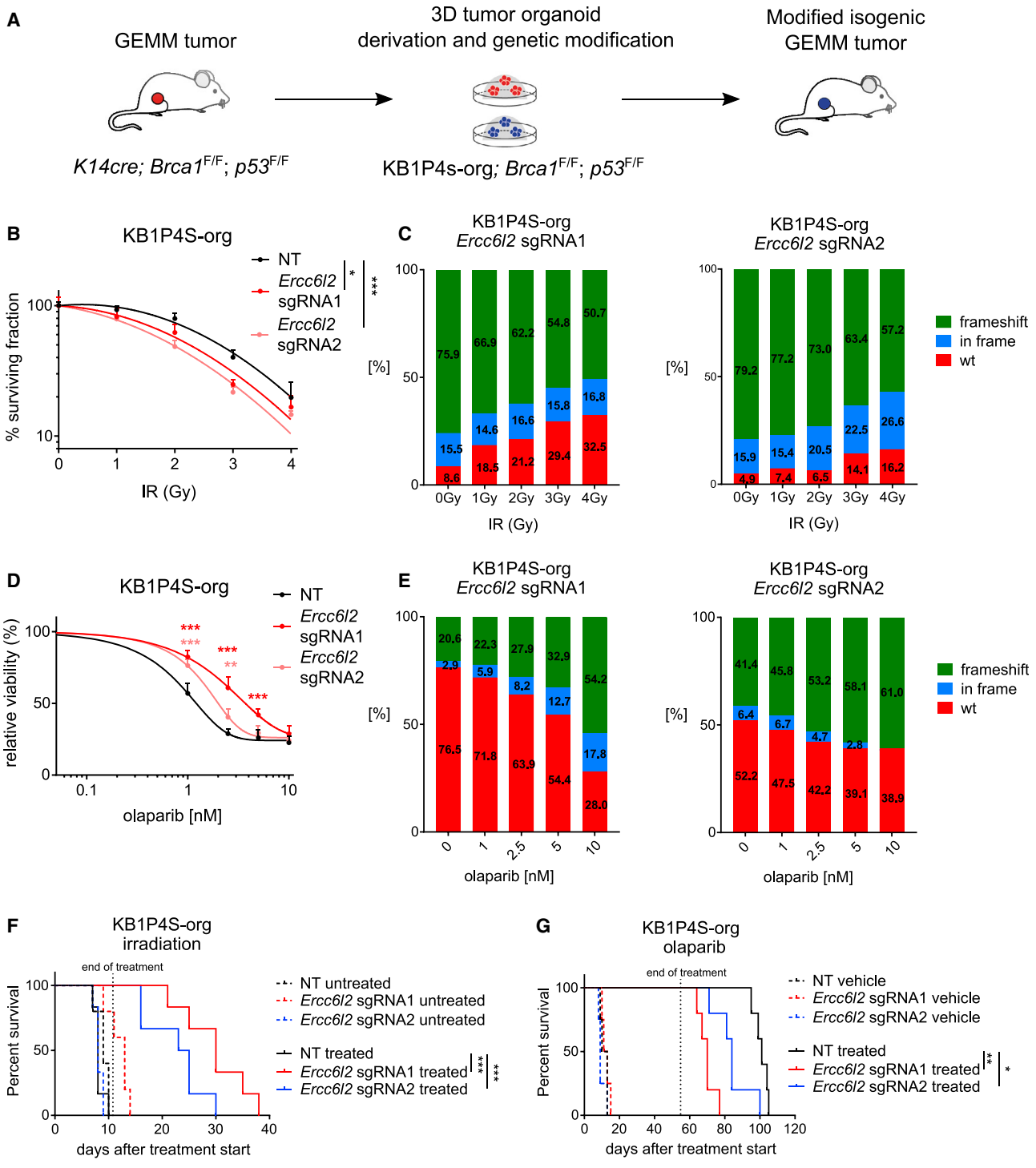

Figure 3. Loss of *Ercc6l2* Induces IR Sensitivity and PARPi Resistance *In Vivo*

(A) Schematic overview of the generation of isogenic *Ercc6l2*-mutated and control tumors by *ex vivo* manipulation of tumor organoids.

(B) IR response of CRISPR-Cas9-targeted KB1P4S organoids with the indicated sgRNAs. Three biological replicates were plotted as mean ± SD and fitted to the linear quadratic survival model. Statistics were calculated using the CFAssay in R. *p < 0.05 ***p < 0.001.

(C) Allelic modification rates of *Ercc6L2*-knockout KB1P4S organoids following IR evaluated by TIDE analysis.

(D) Olaparib response of *Ercc6l2*-knockout KB1P4S organoids. Three biological replicates were plotted as mean ± SD and fitted to the linear quadratic survival model. Statistics were calculated using 2-way ANOVA followed by Dunnett's test. ***p < 0.001.

(legend continued on next page)

that its loss could confer PARPi resistance in BRCA1-deficient cells. To test this prediction, we generated new polyclonal KB1P-G3 lines harboring 50%–60% frameshift modifications in the *Ercc6l2* alleles. Inactivation of *Ercc6l2* with two *Ercc6l2*-targeting sgRNAs in BRCA1-deficient and -proficient polyclonal and monoclonal cells caused resistance toward the PARPi olaparib (Figures 2C, S2I, S2J, S2K, S2L, S2M, and S2P) and talazoparib (Figure S2Q). In contrast to the control cells, ERCC6L2-depleted cells formed resistant colonies after 11 days of PARPi selection. This effect was specific to *Ercc6l2* inactivation, as shown by the TIDE analysis (Figure 2D). In the initial tumor cell population, about half of the alleles carried frameshift mutations. In contrast, PARPi selection resulted in a substantial increase in frameshift disruptions (>90% for sgRNA1 and >70% for sgRNA2), showing that the *Ercc6l2*-mutated cells have a clear survival advantage in the presence of PARPi (Figure 2D). ERCC6L2-loss-mediated PARPi resistance could be partially rescued by complementing KB1P-G3 cells with WT or $Ercc6l2^{\Delta Hebo}$, but not with $Ercc6l2^{\Delta SNF2}$, supporting the important role of the SNF2 domain for ERCC6L2 function (Figures 2G and 2H).

Taken together, these data indicate that inactivation of *Ercc6l2*, similar to the loss of members of the shieldin and CST complexes, causes an increase in both IR sensitivity and PARPi resistance in BRCA1-deficient cells, altogether suggesting the participation of ERCC6L2 in 53BP1-dependent NHEJ.

Loss of *Ercc6l2* Induces IR Sensitivity and PARPi Resistance *In Vivo*

To explore the *in vivo* effects of *Ercc6l2* deficiency on the treatment response of BRCA1-deficient tumors to IR and PARPi, we made use of the mammary tumor organoid technology (Figure 3A; Duarte et al., 2018). Organoid cultures can be easily genetically modified and orthotopically transplanted, giving rise to mammary tumors that preserve the epithelial morphology and drug response of the original tumor. For this purpose, KB1P4S organoids (KB1PS-org), derived from a *K14cre;* $Brca1^{F/F}$;$p53^{F/F}$ (KB1P) mammary tumor, were cultured *ex vivo* and transduced with lentiviruses carrying pLentiCRISPRv2-sg*Ercc6l2*-Puro vectors. Control organoids were generated by transduction with pLentiCRISPR v2-NT sgRNA-Puro lentivirus encoding a NT sgRNA. Organoids were subsequently exposed to IR (3 doses of 1, 2, 3, or 4 Gy over 3 consecutive days) or to olaparib (1, 2.5, 5, or 10 nM) *in vitro*, and their clonogenic capacity was evaluated after 14 days. As expected, organoids targeted by NT sgRNA showed high sensitivity to both IR and PARPi treatment (Figures 3B, 3D, S3A, and S3B). In contrast, *Ercc6l2*-targeted cells showed increased radiosensitivity and resistance to olaparib, corroborating the data obtained with the 2D KB1P-G3 cells (Figures 3B, 3D, S3A, and S3B). Consistent with this finding, quantification of the changes in allele distributions by TIDE analysis showed depletion or enrichment of *Ercc6l2* frameshift mutations following IR and olaparib treatment, respectively (Figures 3C and 3E).

We next examined whether the increased sensitivity to IR caused by *Ercc6l2* loss is exploitable *in vivo*. To this end, the transduced KB1P4S tumor organoids were orthotopically transplanted in mice. Fractionated RT consisting of two consecutive doses of 4 Gy per week for 2 weeks was initiated on mice bearing established tumors (50–100 mm^3) by using a high-precision small animal irradiator equipped with a cone-beam computed tomography (CT) scanner. The effect on tumor volume was measured as depicted in Figure S3C. Depletion of *Ercc6l2* significantly enhanced the response to RT and resulted in a prolonged survival, highlighting the role of ERCC6L2-mediated DNA repair in response to RT (Figure 3F). Moreover, we examined the effect of the loss of *Ercc6l2* on PARP inhibition. Mice carrying BRCA1-deficient mouse mammary tumors derived from KB1P4S organoids were treated daily with vehicle or olaparib for 56 consecutive days when tumors reached a size of 50–100 mm^3. *In vivo Ercc6l2* depletion induced faster tumor regrowth after PARPi treatment and resulted in accelerated mammary tumor-related morbidity (Figures 3G and S3D). The difference to the organoid-derived tumors transduced with NT gRNAs is not as strong as we previously reported for *Trp53bp1*-mutated tumors (Duarte et al., 2018) but was comparable to the level of resistance we detected for those mutated for the *Ctc1* (Barazas et al., 2018), *Shld1*, and *Shld2* genes (Noordermeer et al., 2018).

Depletion of *Ercc6l2* Restores HR in BRCA1-Deficient Cells

Among the PARPi resistance mechanisms identified to date, partial restoration of HR is frequently observed in BRCA1-deficient mouse mammary tumors (Francica and Rottenberg, 2018). In these models, restoration of HR was mainly driven by the loss of members of the 53BP1/RIF1/REV7/shieldin/CST pathway (Barazas et al., 2018; Dev et al., 2018; Jaspers et al., 2013; Mirman et al., 2018; Noordermeer et al., 2018). To examine whether PARPi resistance in *Ercc6l2*-depleted KB1P-G3 cells was also caused by HR restoration, we monitored RAD51 IR-induced foci (IRIF), a surrogate readout of HR proficiency, in these cells by using BRCA1-positive (HR-proficient) KB1P-G3B1+ cells and *Trp53bp1*-depleted (HR-restored) KB1P-G3 cells as controls (Figures 4A and 4B). Indeed, the loss of *Ercc6l2* also restored the ability of BRCA1-deficient cells to support RAD51 IRIF. This capability was lost after reintroducing either the WT or the $Ercc6l2^{\Delta Hebo}$-mutated form of *Ercc6l2* in *Ercc6l2*-depleted KB1P-G3 cells but was still present in the $Ercc6l2^{\Delta SNF2}$ KB1P-G3 mutants (Figures S4A and S4B). These data are consistent with the clonogenic assays depicted in Figure 2H and provide further evidence for the importance of the SNF2/ATPase protein domain for ERCC6L2 function.

We then tested the effect of *Ercc6l2* loss on the HR status in conditional BRCA1-deficient $R26^{CreERT2}$;$Brca1^{SCo/D}$;$Pim1^{DR\text{-}GFP/wt}$ mouse embryonic stem cells (mESCs) carrying a

(E) Allelic modification rates of *Ercc6l2*-knockout KB1P4S organoids upon olaparib treatment evaluated by TIDE analysis.
(F and G) Survival of mice orthotopically transplanted with modified KB1P4S tumor organoids was plotted as Kaplan-Meier curves and analyzed with the log-rank test. *$p < 0.05$, **$p < 0.01$, ***$p < 0.001$.
See also Figure S3.

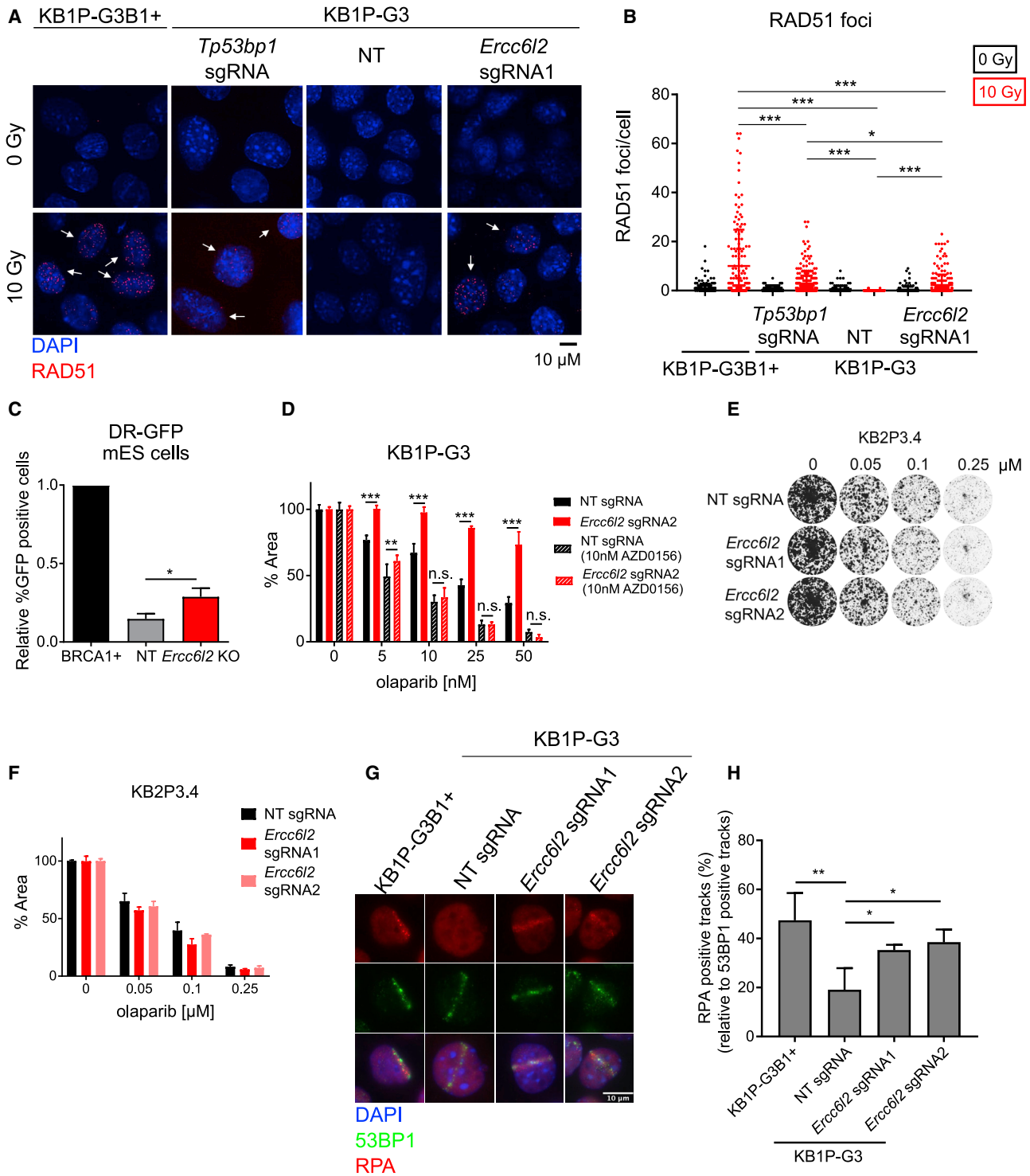

Figure 4. Depletion of *Ercc6l2* Restores HR in BRCA1-Deficient Cells

(A) Representative IRIF immunofluorescence images of KB1P-G3B1+ and KB1-G3 cells modified by CRISPR-Cas9 with the indicated sgRNAs. RAD51-positive cells are highlighted by the white arrows.

(B) Quantification of immunofluorescence staining of RAD51 foci per nucleus. Statistical difference between IRIF on irradiated (red) samples was analyzed by the nonparametric Mann-Whitney test. *p < 0.05, **p < 0.01, ***p < 0.001.

(legend continued on next page)

stably integrated direct repeats green fluorescent protein (DR-GFP) reporter (Bouwman et al., 2013). These cells were transfected to transiently express mCherry and I-SceI, and the percentage of mCherry/GFP double-positive cells was quantified by fluorescence-activated cell sorting (FACS) 24 h later. Switching of the conditional *Brca1*^{SCo} allele impaired HR activity, which was partially rescued upon depletion of *Ercc6l2* (Figure 4C). Also in the non-switched, BRCA1-proficient mESCs, we observed a slight increase in GFP-positive cells when *Ercc6l2* was knocked out (Figure S4C). In contrast to the BRCA1-deficient KB1P-G3 cells, this did not result in a detectable increase in RAD51 IRIF in irradiated isogenic BRCA1-proficient KB1P-G3B1+ cells (Figures S4D and S4E).

In view of further confirming that the PARPi resistance we observed in *Ercc6l2*-mutated KB1P-G3 cells is dependent on HR activation, we selected these cells with olaparib after ATM inhibition. ATM is one of the main kinases promoting HR-dependent DNA repair in the S/G2 phases of the cell cycle (Gupta et al., 2014). As shown in Figure 4D, the ATM inhibitor AZD0156 restored PARPi sensitivity, indicating that ATM-dependent activation of HR is crucial for the survival of PARPi-treated *Ercc6l2*-mutated BRCA1-deficient cells.

In the presence of DNA damage, the resection of DSBs governs the balance between repair by HR (which requires a 3′ single-stranded DNA (ssDNA) overhang and NHEJ (which joins unresected ends) (Setiaputra and Durocher, 2019). This decision is tightly regulated by DNA end protection by 53BP1 pathway proteins, which collectively antagonize resection and promote repair by NHEJ. Conversely, BRCA1 alleviates the resection blocks posed by chromatin-associated 53BP1 pathway proteins, allowing for end resection and DNA repair by HR (Chapman et al., 2012, 2013; Daley and Sung, 2014; Escribano-Díaz et al., 2013; Feng et al., 2015; Noordermeer et al., 2018; Panier and Boulton, 2014). Consequently, in the absence of BRCA1, the block to resection posed by 53BP1 and its effectors (REV7-shieldin and CST) prevents HR, thereby explaining why the loss of these factors causes PARPi resistance (Boersma et al., 2015; Chapman et al., 2013; Mirman et al., 2018; Noordermeer et al., 2018; Xu et al., 2015). Hence, the fact that *Ercc6l2* loss similarly suppressed the synthetic lethal effect of PARPi in BRCA1-deficient cells suggested a potential inhibitory role in DSB end resection. Such a hypothesis was also supported by the fact that depletion of *Ercc6l2* did not restore HR or confer PARPi resistance in *Brca2* knockout cells (Figures 4E, 4F, and S4F), consistent with the fact that 53BP1 pathway loss cannot restore HR in BRCA2-deficient cells (Bouwman et al., 2010).

Based on these results we analyzed whether DNA end resection is altered in the absence of *Ercc6l2 in* BRCA1-deficient cells by using replication protein A (RPA) immunostaining as a surrogate marker of resection-dependent generation of ssDNA tracts. Cells were exposed to laser beam irradiation, and BRCA1 deficiency resulted in a marked decrease in RPA/53BP1 double-positive laser tracks compared to BRCA1-proficient cells. Indicative of proficient resection, *Ercc6l2* depletion in KB1P-G3 cells partially rescued RPA protein accrual at damage sites (Figures 4G and 4H). Although depletion of *Ercc6l2* did not rescue DNA end resection (ssDNA levels) to the same extent as was evident in BRCA1-complemented KB1P-G3 cells, this partial rescue nonetheless corresponds to increased PARPi resistance. Hence, our data indicate that ERCC6L2 antagonizes HR by inhibiting DNA end resection, an effect we predicted might occur by the 53BP1 pathway.

ERCC6L2 Facilitates NHEJ during Class Switch Recombination (CSR)

We thus examined whether ERCC6L2, akin to 53BP1 pathway proteins, could contribute to NHEJ. To this end, we treated BRCA1-deficient KB1P-G3 cells with the DNA-PKcs inhibitor (NU7441), which inhibits NHEJ, and then exposed the cells to IR. Because the addition of NU7441 sensitized parental and *Ercc6l2*-depleted cells to similar levels, the radiosensitivity induced by the loss of *Ercc6l2* is likely mediated by its role in NHEJ repair (Figure 5A). As a measure for physiological NHEJ capacity, we then assessed whether ERCC6L2 depletion in mouse CH12-F3 B cells affected their ability to undergo immunoglobulin (Ig) CSR from IgM to IgA similarly to 53BP1 pathway proteins, which are near-essential for the joining of DSBs formed at the Ig heavy chain (*igh)* locus (Barazas et al., 2018; Chapman et al., 2013; Ghezraoui et al., 2018; Xu et al., 2015; Manis et al., 2002; Ward et al., 2004). B cells deficient in these proteins upon stimulation are unable to efficiently recombine their *igh* and activate the expression of CSR-dependent Ig isotypes. We therefore questioned whether *Ercc6l2* deletion in the murine CH12-F3 B cell lymphoma line impacted their ability to undergo high-efficiency CSR from IgM to IgA (Muramatsu et al., 2000). CH12-F3 B cells were therefore treated with *Ercc6l2*-targeting CRISPR-Cas9 constructs, and multiple isogenic *Ercc6l2*-knockout clones were derived and were each confirmed to harbor bi-allelic transcript-disrupting frameshift mutations. Upon stimulation, the proliferation profile of these clones was indistinguishable from that of WT CH12-F3 B cells (Figure S5A); yet, *Ercc6l2*$^{-/-}$ CH12-F3 lines showed dramatically reduced CSR compared to parental controls and exhibited defects approaching those observed in *Rev7*$^{-/-}$

(C) DR-GFP assay performed on *Ercc6l2* depleted in mESCs. Three biological replicates were plotted as mean ± SD, and statistical significance was calculated using the two-tailed Student's t test. *p < 0.05, **p < 0.01, ***p < 0.001.
(D) Quantification of growth assays with CRISPR-Cas9-modified KB1P-G3 cells in the presence of olaparib or in combination with AZD0156. Data represent mean ± SD including at least three independent repeats. Statistical analysis was done using the two-way ANOVA followed by Dunnett's multiple comparison test. *p < 0.05, ***p < 0.001.
(E) Growth assay using the BRCA2-deficient KB2P3.4 cells modified by CRISPR-Cas9 with the indicated sgRNAs in the presence of olaparib selection.
(F) Quantification of (E).
(G) Representative images of RPA-negative and RPA-positive 53BP1-labeled laser tracks in CRISPR-Cas9-modified KB1P-G3B1+ and KB1-G3 cells. Scale bar, 10 μM.
(H) Quantification of RPA- and 53BP1-positive laser tracks. Four biological replicates were plotted as mean ± SD. Significance was calculated by one-way ANOVA followed by Tukey's multiple comparison test. *p < 0.05, **p < 0.01.
See also Figure S4.

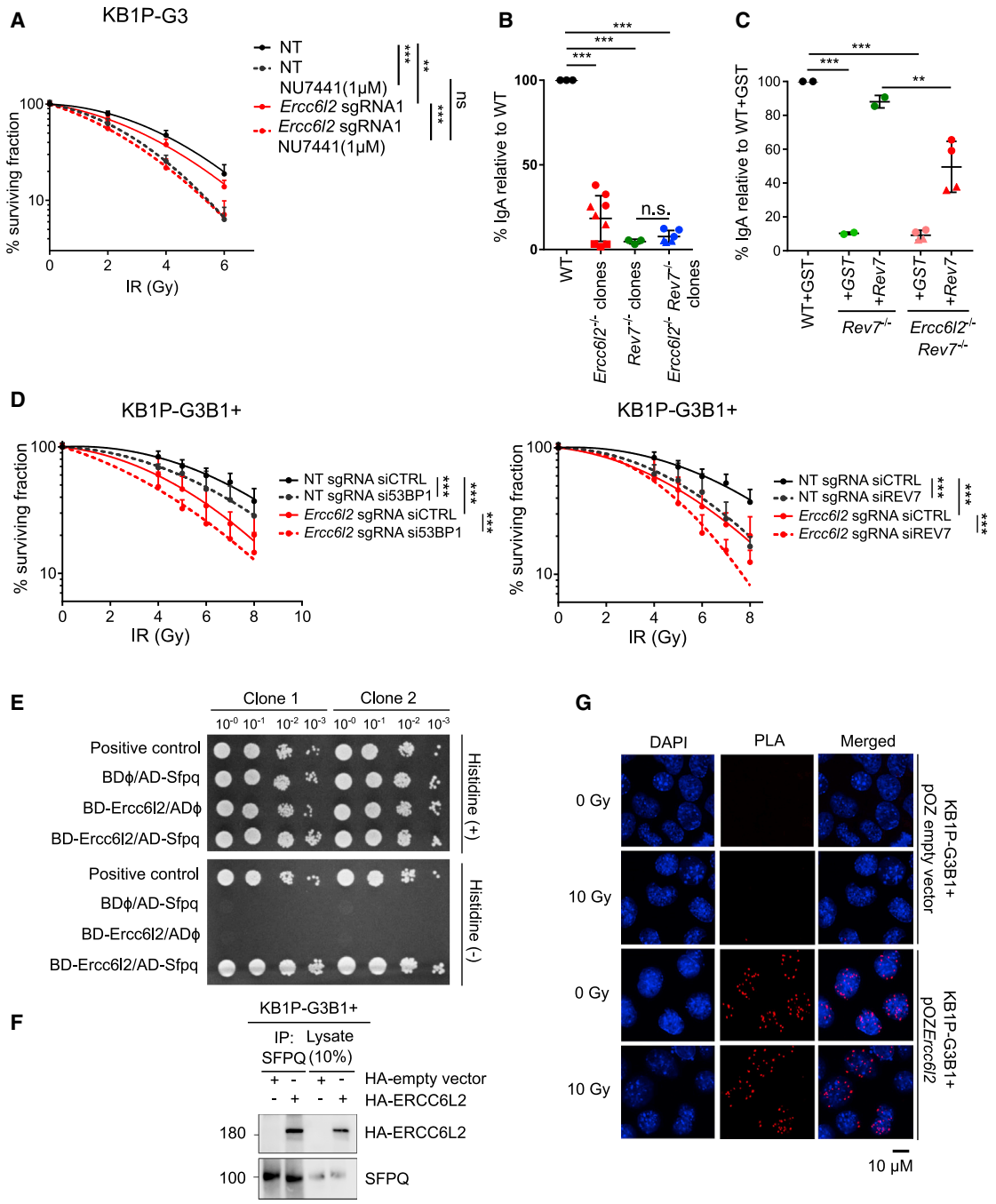

Figure 5. ERCC6L2 Facilitates NHEJ at DSBs

(A) Clonogenic survival of irradiated KB1P-G3 cells modified by CRISPR-Cas9 with the indicated sgRNAs after 1-h treatment with the DNA-PK inhibitor NU7441. Data represent the mean ± SD of at least three independent repeats. Statistics were calculated using the CFAssay in R. $^{**}p < 0.01$, $^{***}p < 0.001$.

(B) Quantification of IgM-to-IgA class switch recombination (CSR) of CRISPR-Cas9-modified CH12-F3 cells 40 h after stimulation with anti-CD40 antibody, interleukin-4 (IL-4), and transforming growth factor β1 (TGF-β1). Within each column, different dot shapes correspond to different CH12-F3 clones. Three biological replicates were plotted as mean ± SD, and statistics were calculated using one-way ANOVA followed by Tukey's multiple comparison test. $^{***}p < 0.001$.

(C) Quantification of IgM-to-IgA CSR of *Rev7*- or *Rev7*/*Ercc6l2*-knockout CH12-F3 cells complemented with the indicated cDNA constructs. Glutathione S-transferase (GST) was used as an inert control. Data represent the mean ± SD of two independent experiments performed in triplicate. Statistics were calculated using one-way ANOVA followed by Tukey's multiple comparison test. $^{***}p < 0.001$.

(D) Proliferation assay of *Ercc6l2*-depleted KB1P-G3B1+ cells treated with the indicated small interfering RNAs (siRNAs) before IR treatment. Data represent the mean ± SD of three independent experiments performed in triplicate. Statistics were calculated using the CFAssay in R. $^{***}p < 0.001$.

(legend continued on next page)

cells (Figures 5B and S5B). To check whether ERCC6L2 might function with 53BP1 pathway proteins during CSR, we generated *Ercc6l2*- and *Rev7*-double knockout CH12-F3 B clones. CSR defects in the resulting *Rev7*$^{-/-}$ *Ercc6l2*$^{-/-}$ CH12-F3 clones were stronger than in *Ercc6l2*$^{-/-}$ clones, yet, were not stronger than the severe defects apparent in *Rev7*$^{-/-}$ cells (Figure 5B). Consistently, reintroduction of stable *Rev7* expression only partially suppressed CSR defects in *Rev7*$^{-/-}$ *Ercc6l2*$^{-/-}$ CH12-F3, in contrast to complemented *Rev7*$^{-/-}$ CH12-F3 clones that exhibited WT IgM to IgA class switching frequencies (Figures 5C and S5C). Although the CSR defects harbored by *Rev7*$^{-/-}$ CH12-F3 are already severe, the fact that residual switching frequencies were not lower in *Rev7*$^{-/-}$ *Ercc6l2*$^{-/-}$ cells is consistent with a role for ERCC6L2 in NHEJ. Nonetheless, the weaker penetrance of CSR defects in *Ercc6l2*$^{-/-}$ cells is suggestive of a direct yet accessory role for ERCC6L2 in promoting NHEJ during CSR, which are results consistent with findings for a recently published *Ercc6l2*$^{-/-}$ mouse model that similarly harbored CSR defects (Liu et al., 2020). In line with these results, knockdown of *Trp53bp1* or *Rev7* in *Ercc6l2*-depleted KB1P-G3 B1+ cells led to an additional sensitivity in response to IR (Figures 5D and S5D), and no direct interaction of ERCC6L2 with 53BP1 or REV7 (Figure S5E) was observed. Moreover, the fact that neither we nor others (Liu et al., 2020) detected an alteration in the stability of other NHEJ factors, including 53BP1, RIF1, REV7, XRCC4, or LIG4 (Figure S5F), furthermore supports a direct contribution of ERCC6L2 to NHEJ.

SFPQ as a Novel Interaction Partner of ERCC6L2

To identify the interacting factors that link ERCC6L2 to DNA end-joining in an unbiased manner, we carried out a yeast two-hybrid (Y2H) screen using a mouse cDNA library and a C-terminal region of ERCC6L2 (amino acids [aa] 885–1360) containing the HEBO domain as bait. By testing more than 51 million interactions, this screen identified 255 clones representing 19 different genes with a high confidence of interaction to ERCC6L2 (Table S4). Among them, SFPQ stood out as the potential link of ERCC6L2 to NHEJ because it is known to promote NHEJ together with non-POU domain-containing octamer-binding protein (NONO) (Bladen et al., 2005; Jaafar et al., 2017; Udayakumar et al., 2003; Udayakumar and Dynan, 2015). Moreover, NONO was also a hit in one of our radiosensitivity screens (Table S2). We therefore tested the interaction of ERCC6L2 with SFPQ in our mouse mammary tumor cells. To this purpose, we first confirmed that both proteins are localized in the nucleus, as shown in Figures S5G and S5H. Notably, for both proteins we did not observe IRIF formation, suggesting that low protein levels are sufficient for their contribution to DNA end-joining. Next, we confirmed the direct interaction of ERCC6L2 with SFPQ by using co-immunoprecipitation. Consistent with the Y2H results as well as the 1-by-1 Y2H validation (Table S4; Figure 5E), SFPQ co-eluted with HA-ERCC6L2 (Figure 5F). We also corroborated these data using the proximity ligation assay (PLA), which showed positive PLA signals in the nuclei of KB1P-G3B1+ cells, independently of the induction of DNA damage (Figure 5G).

Together, these data show that ERCC6L2 not only antagonizes end resection but also contributes to DNA end-joining. Our results suggest that ERCC6L2's NHEJ activity may involve its interaction with SFPQ.

ERCC6L2 Mutations Are Associated with a Low Homologous Recombination Deficiency (HRD) Score and Correlate with a Better Overall Survival in Uterine Corpus Endometrial Carcinoma (UCEC) Patients Treated with RT

To elucidate the importance of *ERCC6L2* mutations in patients, we investigated The Cancer Genome Atlas (TCGA) PanCancer Atlas studies containing more than 10,000 primary tumors and matched normal samples from 33 different cancer types (www.cbioportal.org). Mutations, gene amplifications, deep deletions, and fusions within the *ERCC6L2* gene were reported in various cancer types, including breast (BRCA) and ovarian (OV) cancer, which are treated with PARPi. The presence of point mutations in the *ERCC6L2* gene was the most frequent alteration among all cancer types. In particular, patients from the UCEC cohort most often harbored mutations in the *ERCC6L2* gene (Figure 6A; Table S5). Therefore, we focused our analysis on this cancer type. In this cohort, *ERCC6L2* mRNA expression was significantly higher in normal tissues than in tumors, comprising 176 primary tumors and 24 normal tissues with mRNA expression data (Figure 6B; Table S5). Moreover, tumor-normal matched tissues from 6 UCEC patients showed 0.57 times lower *ERCC6L2* mRNA expression levels in tumor samples ($p = 0.1081$; Figure S6A).

As we uncovered a role for ERCC6L2 in mediating DSB repair, we analyzed the HRD score, which is the sum of scores for telomeric-allelic imbalance (TAI), large-scale transition (LST), and loss-of-heterozygosity (HRD LOH), as previously described (Knijnenburg et al., 2018). UCEC patients harboring an *ERCC6L2* mutation showed significantly lower HRD scores than patients with WT *ERCC6L2* (Figures 6C, S6B, S6C, and S6D; Table S5). Furthermore, a significant negative correlation was observed between the HRD score and the *ERCC6L2* mRNA expression levels in all the cancer tissues of the UCEC cohort (Figure 6D). We further supported these findings by Kyoto encylopedia genes and genomes (KEGG) pathway analysis of *ERCC6L2*-mutant and -WT patients. Gene set enrichment analysis (Subramanian et al., 2005) showed significantly upregulated expression of the genes belonging to the KEGG HR pathway in *ERCC6L2* mutated compared to WT tumor samples (Figure 6E; Table S6). These data suggest that ERCC6L2 deficiency fosters homology-directed DNA repair, which is consistent with a role of ERCC6L2 in blocking end resection.

Because we found ERCC6L2 in the context of IR sensitivity, we then investigated the effect of *ERCC6L2* mutations on the long-term overall survival of patients within the UCEC cohort who received RT. Indeed, we observed that patients harboring *ERCC6L2* mutations in their tumors showed a strikingly longer

(E) A 1-by-1 validation of the ERCC6L2 and SFPQ interaction using the yeast two-hybrid technique in two independent clones.
(F) Western blotting showing the levels of the indicated proteins following immunoprecipitation of HA-tagged ERCC6L2 in KB1P-G3B1+ cells.
(G) Proximity ligation assay showing the ERCC6L2 and SFPQ interaction in KB1P-G3B1+ cells expressing HA-ERCC6L2. Cells were stained 3 h after 10 Gy of IR.
See also Figure S5 and Table S4.

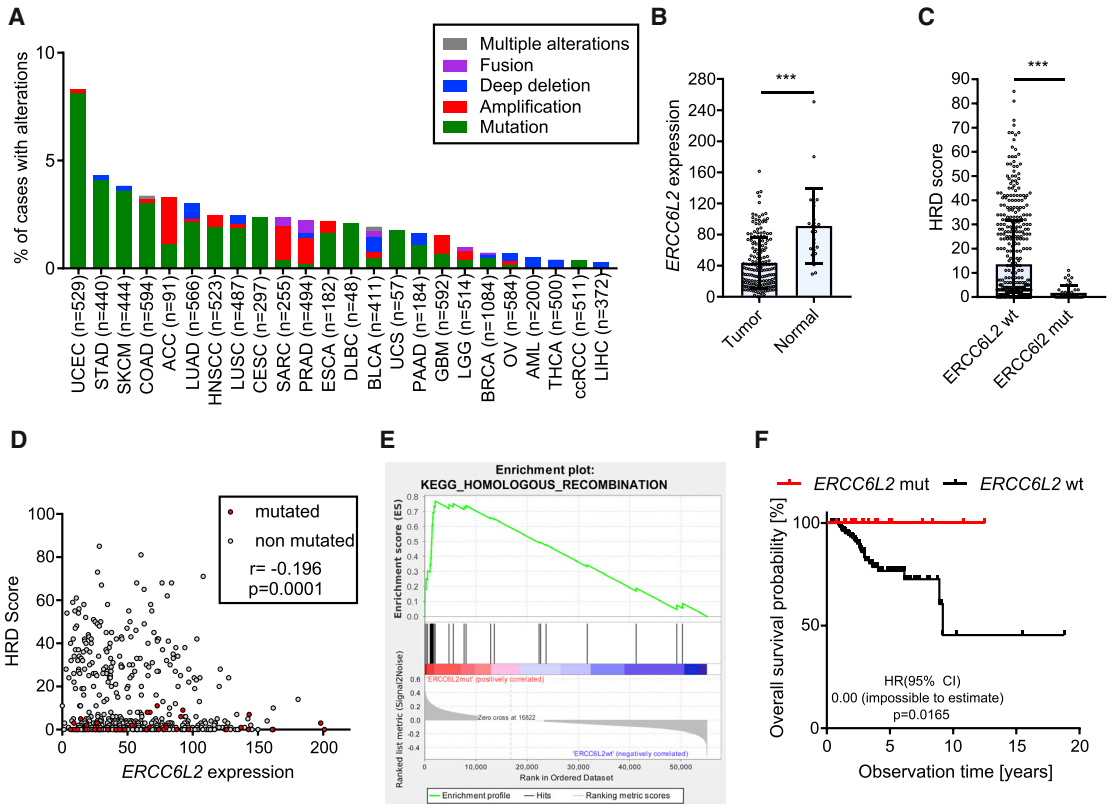

Figure 6. *ERCC6L2* Mutations Are Associated with a Low HR Deficiency (HRD) Score and Correlate with a Better Overall Survival in Uterine Corpus Endometrial Carcinoma (UCEC) Patients Treated with RT

(A) An overview of the frequency of alterations of the *ERCC6L2* gene across all available cohorts. The UCEC cohort contained the greatest number of patients with mutations of *ERCC6L2* (N = 43; Table S5) and was selected for further analyses.

(B) Expression of *ERCC6L2* in solid cancer samples and normal tissue samples from the UCEC cohort of TCGA. Statistical analysis between the two groups was done with unpaired Student's t test. ***p < 0.001.

(C) Association of HRD scores with *ERCC6L2* mutation in the UCEC cohort. Statistical analysis between two groups was done with unpaired Student's t test. ***p < 0.001.

(D) The correlation of HRD score to *ERCC6L2* expression in the UCEC cohort of TCGA. Linear regression was fitted with a 95% confidence interval. Goodness of fit was shown with r value, which is -0.19. ***p < 0.001.

(E) Enrichment plot for KEGG homologous recombination pathway resulting from gene set enrichment analysis between *ERCC6L2*-mutated and *ERCC6L2* wild-type samples in the UCEC cohort. False discovery rate (FDR), q value = 0.034.

(F) Kaplan-Meyer survival curve of patients from the UCEC cohort with or without *ERCC6L2* mutations who have undergone RT. Hazard ratio for *ERCC6L2* mutant patients was 0, with the 95% confidence interval impossible to calculate due to the lack of observed events. Statistical analysis was done by using log-rank test. *p < 0.05.

See also Figure S6 and Tables S5 and S6.

disease-free and overall survival than patients with WT *ERCC6L2* (Figures 6F and S6E), indicating that *ERCC6L2* loss may be clinically relevant.

Hence, our TCGA data analysis shows that *ERCC6L2* mutations are found in a clinically relevant fraction of human tumors and correlate with a better overall survival in patients treated with RT. This finding encourages further clinical investigations to test the usefulness of *ERCC6L2* as a predictive biomarker of RT response.

DISCUSSION

In this study, we have applied functional genome-wide screens to attribute an important role for ERCC6L2 in the cellular response to IR. In dissecting ERCC6L2's function in this capacity, our data are consistent with a regulatory role for ERCC6L2 in DSB repair that is consistent with an accessory function in NHEJ and a potentially associated role in the antagonization of HR. In recent years, the use of chemogenetic profiling has broadened our understanding of molecular mechanisms responsible for chemotherapy (Colic et al., 2019; Gerhards and Rottenberg, 2018) and immunotherapy (Logtenberg et al., 2019; Mezzadra et al., 2017) response. In analogy to this approach, we scrutinized the genome for alterations that affect the response to IR. As expected, this analysis yielded well-known DSB repair factors, including ATM, DNA-PK, and Artemis. The fact that we found members of the CST and shieldin complexes corroborates their importance for genome maintenance. The loss of these complexes causes PARPi resistance in

BRCA1-deficient cells (Barazas et al., 2018; Dev et al., 2018; Mirman et al., 2018; Noordermeer et al., 2018) and together with their synthetic lethality with IR in HAP1 cells is consistent with previous data of the Jackson and our laboratory showing that radiosensitivity is an acquired vulnerability of the PARPi-resistant BRCA1-deficient tumors (Barazas et al., 2019; Dev et al., 2018).

In our search for other factors of similar function, we focused on ERCC6L2 because it is frequently mutated in human cancer and had not been well characterized in the context of DSB repair. Although ERCC6L2 has sequence similarities with Cockayne syndrome complementation group B (CSB) protein (coded by *ERCC6*) and the ERCC6L/PICH helicase, the amino acid identity is not high (34% for CSB and 30% for ERCC6L). In a small short hairpin RNA (shRNA) screen for olaparib resistance using the hits from our radiosensitivity screen (Figure 1) that have not yet been linked to PARPi resistance, we observed ERCC6L2 to be a major hit (data not shown). Indeed, we found that the loss of ERCC6L2 results in phenotypes consistent with defects affecting the 53BP1-RIF-REV7-shieldin-CST pathway but with less penetrance than cells lacking 53BP1 or its core effectors, such as REV7. In addition to the increased radiosensitivity, our data show that ERCC6L2 loss can alleviate, at least in part, PARPi resistance in BRCA1- but not in BRCA2-deficient cells. Our data are consistent with a role of ERCC6L2 in blocking DNA end resection, and akin to other factors in the 53BP1 pathway that perform an equivalent function, its depletion triggers BRCA1-independent HR restoration. Although HR efficacy is not restored to the same level as in BRCA1-complemented cells, we find it to be sufficient to confer PARPi resistance in cells and in pre-clinical tumor models. Another similarity is the severe defect in CSR we found to accompany *ERCC6L2*-deletion in B cells, an effect consistent with immunodeficiencies in ERCC6L2-deficient mice reported while this work was in revision (Liu et al., 2020).

How ERCC6L2, a putative chromatin remodeler, precisely contributes to NHEJ remains to be determined. Our observation that it interacts with SFPQ, a member of the SFPQ-NONO complex that has only recently been attributed a putative functions in NHEJ, may offer some clues. The SFPQ-NONO complex has been shown to cooperate with the Ku protein at an early step of NHEJ, where it forms a stable pre-ligation complex and stimulates end joining (Bladen et al., 2005). Perhaps, ERCC6L2-dependent nucleosome remodeling could assist the formation of the functional pre-ligation complex within a chromatinized template, thereby allowing for the efficient alignment of separate DNA molecules. Indeed, further complex biochemical studies will be needed to test these predictions and define the precise function of ERCC6L2 in NHEJ.

In addition to ERCC6L2, our radiogenetic screens provided other genes for which more detailed follow-up analyses may give new insights into radiobiology. For example, MND1 is well known for its role in proper homologous chromosome pairing and efficient cross-over and intragenic recombination during meiosis (Sansam and Pezza, 2015). As a major hit in our screen, MND1 may have an additional role independent of meiosis and contribute significantly to fixing IR-induced damage using homology-directed repair.

In contrast to the platinum- or microtubule-targeting drugs that we tested previously by using insertional mutagenesis profiling in haploid cells (Gerhards et al., 2018; Planells-Cases et al., 2015), our screens did not yield reproducible gene knockouts that provide a growth advantage in the presence of IR. Although this result may be due to the short IR selection period of 10 days, it suggests that gain-of-function mutations may be more relevant to explain radioresistance.

Regarding the clinical translation, our screen has yielded various proteins that are frequently mutated in human cancers and may be useful predictive markers for RT response as we show for ERCC6L2. Importantly, several of these genes are not essential or only essential for the growth of some cell types, like ERCC6L2 in bone-marrow-derived cells. Hence, in addition to ATM and DNA-PK inhibitors that are currently tested in the clinic with RT, our functional profiling may provide useful targets for the development of potent radiosensitizers.

STAR★METHODS

Detailed methods are provided in the online version of this paper and include the following:

- KEY RESOURCES TABLE
- RESOURCE AVAILABILITY
  - Lead Contact
  - Materials Availability
  - Data and Code Availability
- EXPERIMENTAL MODEL AND SUBJECT DETAILS
  - Mice
  - Cell Lines
  - Tumor-Derived Organoids
- METHOD DETAILS
  - Haploid Genetic screens
  - STRING Analysis
  - Gene editing, silencing, plasmids, and cloning
  - gDNA isolation, amplification, and TIDE analysis
  - Clonogenic assays
  - Growth assays
  - Western blotting
  - *In vivo* studies
  - Immunoflorescence staining and RAD51 irradiation induced foci (IRIF) analysis
  - Proximity ligation assay (PLA)
  - DR-GFP Assay
  - RPA loading assay
  - CSR Assay
  - CH12-F3 proliferation assay
  - Immunoprecipitation
  - Yeast two–hybrid screen
  - TCGA data analysis
  - Data acquisition and preparation
  - HRD Score and ERCC6L2 mRNA expression correlation in samples from the TCGA UCEC cohort
  - Comparison of the ERCC6L2 mRNA expression between solid tumor and normal samples from the TCGA UCEC cohort
  - Comparison of HRD Score and its constituents between ERCC6L2mut and ERCC6L2wt samples

- Assessment of the clinical impact of ERCC6L2 mutations on the overall and disease-specific survival in TCGA UCEC patients—univariate analysis
- Gene set enrichment analysis

- QUANTIFICATION AND STATISTICAL ANALYSIS
  - Haploid Genetic screens
  - Clonogenic Assays
  - Growth Assays
  - *In vivo* studies
  - RAD51 IRIF analysis
  - DR-GFP Assay
  - CSR Assay
  - RPA loading assay
  - TCGA data analysis

SUPPLEMENTAL INFORMATION

Supplemental Information can be found online at https://doi.org/10.1016/j.celrep.2020.108068.

ACKNOWLEDGMENTS

We wish to thank Piet Borst, Martin Liptay, Joana Santos Barbosa, and Kerry Woods for critical reading of the manuscript. Moreover, we thank the members of the Preclinical Intervention Unit of the Mouse Clinic for Cancer and Ageing (MCCA) at the Netherlands Cancer Institute (NKI) and Myriam Siffert, Georgina Lackner, and Fabiana Steck for their help at the Vetsuisse Faculty mouse facility. We are also grateful to Elmer Stickel (NKI) for his bioinformatic support, to Michaela Medová and Yitzhak Zimmer for their technical support, and to the Department for BioMedical Research (DBMR) of the University of Bern for providing the Gammacell 40 irradiator (MDSNordion). Financial support came from the Swiss National Science Foundation (310030_179360 to S.R.), the European Research Council (CoG-681572 to S.R.), Foundation for Polish Science (First TEAM POIR.04.04.00-00-2280/16 to W.F.), the Dutch Cancer Society (NKI 2015-7877 to P.B.), the Swiss Cancer League (KLS-4282-08-2017 to S.R. and KFS-4702-02-2019 to A.A.S.), the Bernese Cancer League (to P.F.), the Novartis Science Foundation (to S.R.), the Wilhelm-Sander Foundation (to S.R.), Cancer Research UK (C52690/A19270 to J.R.C.), and the Forschungskredit of the University of Zurich (FK-19-037 to A.T.).

AUTHOR CONTRIBUTIONS

Conceptualization, P.F., M.M., and S.R.; Methodology, P.F., M.M., V.A.B., A.T., and P.B.; Investigation, P.F., M.M., C.O., Z.N., A.T., P.B., E.S., M.L.H., L.L., I.K., R.d.K.-G., and D.H.; Software and Formal Analysis, P.F., M.M., V.A.B., C.O., Z.N., A.T., P.B., E.S., and M.L.H.; Resources, V.A.B., N.M.G., Z.N., and W.F.; Writing, P.F., M.M., J.R.C., and S.R.; Supervision, M.v.d.V., J.J., A.A.S., W.F., J.R.C., T.B., and S.R.; Funding Acquisition, P.F., J.J., A.A.S., J.R.C., and S.R.

DECLARATION OF INTERESTS

The authors declare no competing interests.

Received: December 18, 2019
Revised: April 27, 2020
Accepted: August 4, 2020
Published: August 25, 2020

REFERENCES

Alhamidi, M., Kjeldsen Buvang, E., Fagerheim, T., Brox, V., Lindal, S., Van Ghelue, M., and Nilssen, Ø. (2011). Fukutin-related protein resides in the Golgi cisternae of skeletal muscle fibres and forms disulfide-linked homodimers via an N-terminal interaction. PLoS One *6*, e22968.

Bagga, M., Kaur, A., Westermarck, J., and Abankwa, D. (2014). ColonyArea: An ImageJ Plugin to Automatically Quantify Colony Formation in Clonogenic Assays. PLoS One *9*, 14–17.

Barazas, M., Annunziato, S., Pettitt, S.J., de Krijger, I., Ghezraoui, H., Roobol, S.J., Lutz, C., Frankum, J., Song, F.F., Brough, R., et al. (2018). The CST Complex Mediates End Protection at Double-Strand Breaks and Promotes PARP Inhibitor Sensitivity in BRCA1-Deficient Cells. Cell Rep. *23*, 2107–2118.

Barazas, M., Gasparini, A., Huang, Y., Küçükosmanoğlu, A., Annunziato, S., Bouwman, P., Sol, W., Kersbergen, A., Proost, N., de Korte-Grimmerink, R., et al. (2019). Radiosensitivity Is an Acquired Vulnerability of PARPi-Resistant BRCA1-Deficient Tumors. Cancer Res. *79*, 452–460.

Barton, M.B., Jacob, S., Shafiq, J., Wong, K., Thompson, S.R., Hanna, T.P., and Delaney, G.P. (2014). Estimating the demand for radiotherapy from the evidence: a review of changes from 2003 to 2012. Radiother. Oncol. *112*, 140–144.

Bladen, C.L., Udayakumar, D., Takeda, Y., and Dynan, W.S. (2005). Identification of the polypyrimidine tract binding protein-associated splicing factor.p54(nrb) complex as a candidate DNA double-strand break rejoining factor. J. Biol. Chem. *280*, 5205–5210.

Blomen, V.A., Májek, P., Jae, L.T., Bigenzahn, J.W., Nieuwenhuis, J., Staring, J., Sacco, R., van Diemen, F.R., Olk, N., Stukalov, A., et al. (2015). Gene essentiality and synthetic lethality in haploid human cells. Science *350*, 1092–1096.

Bluteau, O., Sebert, M., Leblanc, T., Peffault de Latour, R., Quentin, S., Lainey, E., Hernandez, L., Dalle, J.H., Sicre de Fontbrune, F., Lengline, E., et al. (2018). A landscape of germ line mutations in a cohort of inherited bone marrow failure patients. Blood *131*, 717–732.

Boersma, V., Moatti, N., Segura-Bayona, S., Peuscher, M.H., van der Torre, J., Wevers, B.A., Orthwein, A., Durocher, D., and Jacobs, J.J.L. (2015). MAD2L2 controls DNA repair at telomeres and DNA breaks by inhibiting 5′ end resection. Nature *521*, 537–540.

Bouwman, P., Aly, A., Escandell, J.M., Pieterse, M., Bartkova, J., van der Gulden, H., Hiddingh, S., Thanasoula, M., Kulkarni, A., Yang, Q., et al. (2010). 53BP1 loss rescues BRCA1 deficiency and is associated with triple-negative and BRCA-mutated breast cancers. Nat. Struct. Mol. Biol. *17*, 688–695.

Bouwman, P., van der Gulden, H., van der Heijden, I., Drost, R., Klijn, C.N., Prasetyanti, P., Pieterse, M., Wientjens, E., Seibler, J., Hogervorst, F.B.L., and Jonkers, J. (2013). A high-throughput functional complementation assay for classification of BRCA1 missense variants. Cancer Discov. *3*, 1142–1155.

Braselmann, H., Michna, A., Heß, J., and Unger, K. (2015). CFAssay: statistical analysis of the colony formation assay. Radiat. Oncol. *10*, 223.

Brinkman, E.K., Chen, T., Amendola, M., and van Steensel, B. (2014). Easy quantitative assessment of genome editing by sequence trace decomposition. Nucleic Acids Res. *42*, e168.

Chapman, J.R., Sossick, A.J., Boulton, S.J., and Jackson, S.P. (2012). BRCA1-associated exclusion of 53BP1 from DNA damage sites underlies temporal control of DNA repair. J. Cell Sci. *125*, 3529–3534.

Chapman, J.R., Barral, P., Vannier, J.B., Borel, V., Steger, M., Tomas-Loba, A., Sartori, A.A., Adams, I.R., Batista, F.D., and Boulton, S.J. (2013). RIF1 is essential for 53BP1-dependent nonhomologous end joining and suppression of DNA double-strand break resection. Mol. Cell *49*, 858–871.

Ciccia, A., and Elledge, S.J. (2010). The DNA damage response: making it safe to play with knives. Mol. Cell *40*, 179–204.

Colaprico, A., Silva, T.C., Olsen, C., Garofano, L., Cava, C., Garolini, D., Sabedot, T.S., Malta, T.M., Pagnotta, S.M., Castiglioni, I., et al. (2016). TCGAbiolinks: an R/Bioconductor package for integrative analysis of TCGA data. Nucleic Acids Res. *44*, e71.

Colic, M., Wang, G., Zimmermann, M., Mascall, K., McLaughlin, M., Bertolet, L., Lenoir, W.F., Moffat, J., Angers, S., Durocher, D., and Hart, T. (2019). Identifying chemogenetic interactions from CRISPR screens with drugZ. Genome Med. *11*, 52.

Daley, J.M., and Sung, P. (2014). 53BP1, BRCA1, and the choice between recombination and end joining at DNA double-strand breaks. Mol. Cell. Biol. *34*, 1380–1388.

Delaney, G., Jacob, S., Featherstone, C., and Barton, M. (2005). The role of radiotherapy in cancer treatment: estimating optimal utilization from a review of evidence-based clinical guidelines. Cancer *104*, 1129–1137.

Dev, H., Chiang, T.-W.W., Lescale, C., de Krijger, I., Martin, A.G., Pilger, D., Coates, J., Sczaniecka-Clift, M., Wei, W., Ostermaier, M., et al. (2018). Shieldin complex promotes DNA end-joining and counters homologous recombination in BRCA1-null cells. Nat. Cell Biol. *20*, 954–965.

Douglas, S.P.M., Siipola, P., Kovanen, P.E., Pyörälä, M., Kakko, S., Savolainen, E.-R., Salmenniemi, U., Orte, K., Kytölä, S., Pitkänen, E., et al. (2019). *ERCC6L2* defines a novel entity within inherited acute myeloid leukemia. Blood *133*, 2724–2728.

Duarte, A.A., Gogola, E., Sachs, N., Barazas, M., Annunziato, S., R de Ruiter, J., Velds, A., Blatter, S., Houthuijzen, J.M., van de Ven, M., et al. (2018). BRCA-deficient mouse mammary tumor organoids to study cancer-drug resistance. Nat. Methods *15*, 134–140.

Eid, W., Steger, M., El-Shemerly, M., Ferretti, L.P., Peña-Diaz, J., König, C., Valtorta, E., Sartori, A.A., and Ferrari, S. (2010). DNA end resection by CtIP and exonuclease 1 prevents genomic instability. EMBO Rep. *11*, 962–968.

Escribano-Díaz, C., Orthwein, A., Fradet-Turcotte, A., Xing, M., Young, J.T.F., Tkáč, J., Cook, M.A., Rosebrock, A.P., Munro, M., Canny, M.D., et al. (2013). A cell cycle-dependent regulatory circuit composed of 53BP1-RIF1 and BRCA1-CtIP controls DNA repair pathway choice. Mol. Cell *49*, 872–883.

Evers, B., Drost, R., Schut, E., de Bruin, M., van der Burg, E., Derksen, P.W.B., Holstege, H., Liu, X., van Drunen, E., Beverloo, H.B., et al. (2008). Selective inhibition of BRCA2-deficient mammary tumor cell growth by AZD2281 and cisplatin. Clin. Cancer Res. *14*, 3916–3925.

Feng, L., Li, N., Li, Y., Wang, J., Gao, M., Wang, W., and Chen, J. (2015). Cell cycle-dependent inhibition of 53BP1 signaling by BRCA1. Cell Discov. *1*, 15019.

Findlay, S., Heath, J., Luo, V.M., Malina, A., Morin, T., Coulombe, Y., Djerir, B., Li, Z., Samiei, A., Simo-Cheyou, E., et al. (2018). SHLD2/FAM35A co-operates with REV7 to coordinate DNA double-strand break repair pathway choice. EMBO J. *37*, e100158.

Francica, P., and Rottenberg, S. (2018). Mechanisms of PARP inhibitor resistance in cancer and insights into the DNA damage response. Genome Med. *10*, 101.

Gao, S., Feng, S., Ning, S., Liu, J., Zhao, H., Xu, Y., Shang, J., Li, K., Li, Q., Guo, R., and Xu, D. (2018). An OB-fold complex controls the repair pathways for DNA double-strand breaks. Nat. Commun. *9*, 3925.

Gerhards, N.M., and Rottenberg, S. (2018). New tools for old drugs: Functional genetic screens to optimize current chemotherapy. Drug Resist. Updat. *36*, 30–46.

Gerhards, N.M., Blomen, V.A., Mutlu, M., Nieuwenhuis, J., Howald, D., Guyader, C., Jonkers, J., Brummelkamp, T.R., and Rottenberg, S. (2018). Haploid genetic screens identify genetic vulnerabilities to microtubule-targeting agents. Mol. Oncol. *12*, 953–971.

Ghezraoui, H., Oliveira, C., Becker, J.R., Bilham, K., Moralli, D., Anzilotti, C., Fischer, R., Deobagkar-Lele, M., Sanchiz-Calvo, M., Fueyo-Marcos, E., et al. (2018). 53BP1 cooperation with the REV7-shieldin complex underpins DNA structure-specific NHEJ. Nature *560*, 122–127.

Gogola, E., Duarte, A.A., de Ruiter, J.R., Wiegant, W.W., Schmid, J.A., de Bruijn, R., James, D.I., Guerrero Llobet, S., Vis, D.J., Annunziato, S., et al. (2018). Selective Loss of PARG Restores PARylation and Counteracts PARP Inhibitor-Mediated Synthetic Lethality. Cancer Cell *33*, 1078–1093.e12.

Gupta, A., Hunt, C.R., Hegde, M.L., Chakraborty, S., Chakraborty, S., Udayakumar, D., Horikoshi, N., Singh, M., Ramnarain, D.B., Hittelman, W.N., et al. (2014). MOF phosphorylation by ATM regulates 53BP1-mediated double-strand break repair pathway choice. Cell Rep. *8*, 177–189.

Gupta, R., Somyajit, K., Narita, T., Maskey, E., Stanlie, A., Kremer, M., Typas, D., Lammers, M., Mailand, N., Nussenzweig, A., et al. (2018). DNA Repair Network Analysis Reveals Shieldin as a Key Regulator of NHEJ and PARP Inhibitor Sensitivity. Cell *173*, 972–988.e23.

He, Y.J., Meghani, K., Caron, M.-C., Yang, C., Ronato, D.A., Bian, J., Sharma, A., Moore, J., Niraj, J., Detappe, A., et al. (2018). DYNLL1 binds to MRE11 to limit DNA end resection in BRCA1-deficient cells. Nature *563*, 522–526.

Jaafar, L., Li, Z., Li, S., and Dynan, W.S. (2017). SFPQ●NONO and XLF function separately and together to promote DNA double-strand break repair via canonical nonhomologous end joining. Nucleic Acids Res. *45*, 1848–1859.

Jackson, S.P., and Bartek, J. (2009). The DNA-damage response in human biology and disease. Nature *461*, 1071–1078.

Jae, L.T., Raaben, M., Riemersma, M., van Beusekom, E., Blomen, V.A., Velds, A., Kerkhoven, R.M., Carette, J.E., Topaloglu, H., Meinecke, P., et al. (2013). Deciphering the glycosylome of dystroglycanopathies using haploid screens for lassa virus entry. Science *340*, 479–483.

Järviaho, T., Halt, K., Hirvikoski, P., Moilanen, J., Möttönen, M., and Niinimäki, R. (2018). Bone marrow failure syndrome caused by homozygous frameshift mutation in the ERCC6L2 gene. Clin. Genet. *93*, 392–395.

Jaspers, J.E., Kersbergen, A., Boon, U., Sol, W., van Deemter, L., Zander, S.A., Drost, R., Wientjens, E., Ji, J., Aly, A., et al. (2013). Loss of 53BP1 causes PARP inhibitor resistance in Brca1-mutated mouse mammary tumors. Cancer Discov. *3*, 68–81.

Knijnenburg, T.A., Wang, L., Zimmermann, M.T., Chambwe, N., Gao, G.F., Cherniack, A.D., Fan, H., Shen, H., Way, G.P., Greene, C.S., et al. (2018). Genomic and Molecular Landscape of DNA Damage Repair Deficiency across The Cancer Genome Atlas. Cell Rep. *23*, 239–254.e6.

Liu, J., Lichtenberg, T., Hoadley, K.A., Poisson, L.M., Lazar, A.J., Cherniack, A.D., Kovatich, A.J., Benz, C.C., Levine, D.A., Lee, A.V., et al. (2018). An Integrated TCGA Pan-Cancer Clinical Data Resource to Drive High-Quality Survival Outcome Analytics. Cell *173*, 400–416.e11.

Liu, X., Liu, T., Shang, Y., Dai, P., Zhang, W., Lee, B.J., Huang, M., Yang, D., Wu, Q., Liu, L.D., et al. (2020). ERCC6L2 Promotes DNA Orientation-Specific Recombination in Mammalian Cells. Cell Res. Published online April 30, 2020. https://doi.org/10.1038/s41422-020-0328-3.

Logtenberg, M.E.W., Jansen, J.H.M., Raaben, M., Toebes, M., Franke, K., Brandsma, A.M., Matlung, H.L., Fauster, A., Gomez-Eerland, R., Bakker, N.A.M., et al. (2019). Glutaminyl cyclase is an enzymatic modifier of the CD47- SIRPα axis and a target for cancer immunotherapy. Nat. Med. *25*, 612–619.

Lord, C.J., and Ashworth, A. (2012). The DNA damage response and cancer therapy. Nature *481*, 287–294.

Pennell, C.A., Arnold, L.W., Lutzt, P.M., Locasciot, N.J., Willoughby, P.B., and Haughton, G. (1985). Cross-reactive idiotypes and common antigen binding specificities expressed by a series of murine B-cell lymphomas: Etiological implications. Proc. Natl. Acad. Sci. USA *82*, 3799–3803.

Manis, J.P., Dudley, D., Kaylor, L., and Alt, F.W. (2002). IgH class switch recombination to IgG1 in DNA-PKcs-deficient B cells. Immunity *16*, 607–617.

Mezzadra, R., Sun, C., Jae, L.T., Gomez-Eerland, R., de Vries, E., Wu, W., Logtenberg, M.E.W., Slagter, M., Rozeman, E.A., Hofland, I., et al. (2017). Identification of CMTM6 and CMTM4 as PD-L1 protein regulators. Nature *549*, 106–110.

Mirman, Z., Lottersberger, F., Takai, H., Kibe, T., Gong, Y., Takai, K., Bianchi, A., Zimmermann, M., Durocher, D., and de Lange, T. (2018). 53BP1-RIF1-shieldin counteracts DSB resection through CST- and Polα-dependent fill-in. Nature *560*, 112–116.

Muramatsu, M., Kinoshita, K., Fagarasan, S., Yamada, S., Shinkai, Y., and Honjo, T. (2000). Class switch recombination and hypermutation require activation-induced cytidine deaminase (AID), a potential RNA editing enzyme. Cell *102*, 553–563.

Nickoloff, J.A., Jones, D., Lee, S.-H., Williamson, E.A., and Hromas, R. (2017). Drugging the Cancers Addicted to DNA Repair. J. Natl. Cancer Inst. *109*, djx059.

Noordermeer, S.M., Adam, S., Setiaputra, D., Barazas, M., Pettitt, S.J., Ling, A.K., Olivieri, M., Álvarez-Quilón, A., Moatti, N., Zimmermann, M., et al.

(2018). The shieldin complex mediates 53BP1-dependent DNA repair. Nature *560*, 117–121.

Panier, S., and Boulton, S.J. (2014). Double-strand break repair: 53BP1 comes into focus. Nat. Rev. Mol. Cell Biol. *15*, 7–18.

Planells-Cases, R., Lutter, D., Guyader, C., Gerhards, N.M., Ullrich, F., Elger, D.A., Kucukosmanoglu, A., Xu, G., Voss, F.K., Reincke, S.M., et al. (2015). Subunit composition of VRAC channels determines substrate specificity and cellular resistance to Pt-based anti-cancer drugs. EMBO J. *34*, 2993–3008.

Reid, L.J., Shakya, R., Modi, A.P., Lokshin, M., Cheng, J., Jasin, M., Baer, R., and Ludwig, T. (2008). E3 ligase activity of BRCA1 is not essential for mammalian cell viability or homology-directed repair of double-strand DNA breaks. Proc. Natl. Acad. Sci. USA *105*, 20876-81.

Sanjana, N.E., Shalem, O., and Zhang, F. (2014). Improved vectors and genome-wide libraries for CRISPR screening. Nat. Methods *11*, 783–784.

Sansam, C.L., and Pezza, R.J. (2015). Connecting by breaking and repairing: mechanisms of DNA strand exchange in meiotic recombination. FEBS J. *282*, 2444–2457.

Schimmel, J., van Schendel, R., den Dunnen, J.T., and Tijsterman, M. (2019). Templated Insertions: A Smoking Gun for Polymerase Theta-Mediated End Joining. Trends Genet. *35*, 632–644.

Schindelin, J., Arganda-carreras, I., Frise, E., Kaynig, V., Longair, M., Pietzsch, T., Preibisch, S., Rueden, C., Saalfeld, S., Schmid, B., et al. (2019). Fiji : an open-source platform for biological-image analysis. Nat. Methods *9*, 676–682.

Schneider, C.A., Rasband, W.S., and Eliceiri, K.W. (2012). NIH Image to ImageJ: 25 years of image analysis. Nat. Methods *9*, 671–675.

Setiaputra, D., and Durocher, D. (2019). Shieldin—the protector of DNA ends. EMBO Rep. *20*, e47560.

Shabanova, I., Cohen, E., Cada, M., Vincent, A., Cohn, R.D., and Dror, Y. (2018). ERCC6L2-associated inherited bone marrow failure syndrome. Mol. Genet. Genomic Med. *6*, 463–468.

Sishc, B.J., and Davis, A.J. (2017). The role of the core non-homologous end joining factors in carcinogenesis and cancer. Cancers (Basel) *9*, 81.

Subramanian, A., Tamayo, P., Mootha, V.K., Mukherjee, S., Ebert, B.L., Gillette, M.A., Paulovich, A., Pomeroy, S.L., Golub, T.R., Lander, E.S., and Mesirov, J.P. (2005). Gene set enrichment analysis: a knowledge-based approach for interpreting genome-wide expression profiles. Proc. Natl. Acad. Sci. USA *102*, 15545–15550.

Szklarczyk, D., Gable, A.L., Lyon, D., Junge, A., Wyder, S., Huerta-cepas, J., Simonovic, M., Doncheva, N.T., Morris, J.H., Bork, P., et al. (2019). STRING v11 : protein–protein association networks with increased coverage, supporting functional discovery in genome-wide experimental datasets. Nucleic Acids Res. *47*, D607–D613.

Tkáč, J., Xu, G., Adhikary, H., Young, J.T.F., Gallo, D., Escribano-Díaz, C., Krietsch, J., Orthwein, A., Munro, M., Sol, W., et al. (2016). HELB Is a Feedback Inhibitor of DNA End Resection. Mol. Cell *61*, 405–418.

Tomida, J., Takata, K.I., Bhetawal, S., Person, M.D., Chao, H.P., Tang, D.G., and Wood, R.D. (2018). FAM35A associates with REV7 and modulates DNA damage responses of normal and BRCA1-defective cells. EMBO J. *37*, e99543.

Trenner, A., and Sartori, A.A. (2019). Harnessing DNA double-strand break repair for cancer treatment. Front. Oncol. *9*, 1388.

Tummala, H., Kirwan, M., Walne, A.J., Hossain, U., Jackson, N., Pondarre, C., Plagnol, V., Vulliamy, T., and Dokal, I. (2014). ERCC6L2 mutations link a distinct bone-marrow-failure syndrome to DNA repair and mitochondrial function. Am. J. Hum. Genet. *94*, 246–256.

Udayakumar, D., and Dynan, W.S. (2015). Characterization of DNA binding and pairing activities associated with the native SFPQ·NONO DNA repair protein complex. Biochem. Biophys. Res. Commun. *463*, 473–478.

Udayakumar, D., Bladen, C.L., Hudson, F.Z., and Dynan, W.S. (2003). Distinct pathways of nonhomologous end joining that are differentially regulated by DNA-dependent protein kinase-mediated phosphorylation. J. Biol. Chem. *278*, 41631–41635.

Ward, I.M., Reina-San-Martin, B., Olaru, A., Minn, K., Tamada, K., Lau, J.S., Cascalho, M., Chen, L., Nussenzweig, A., Livak, F., et al. (2004). 53BP1 is required for class switch recombination. J. Cell Biol. *165*, 459–464.

Wijdeven, R.H., Pang, B., van der Zanden, S.Y., Qiao, X., Blomen, V., Hoogstraat, M., Lips, E.H., Janssen, L., Wessels, L., Brummelkamp, T.R., and Neefjes, J. (2015). Genome-Wide Identification and Characterization of Novel Factors Conferring Resistance to Topoisomerase II Poisons in Cancer. Cancer Res. *75*, 4176–4187.

Xu, G., Chapman, J.R., Brandsma, I., Yuan, J., Mistrik, M., Bouwman, P., Bartkova, J., Gogola, E., Warmerdam, D., Barazas, M., et al. (2015). REV7 counteracts DNA double-strand break resection and affects PARP inhibition. Nature *521*, 541–544.

Zhang, S., Pondarre, C., Pennarun, G., Labussiere-Wallet, H., Vera, G., France, B., Chansel, M., Rouvet, I., Revy, P., Lopez, B., et al. (2016). A nonsense mutation in the DNA repair factor Hebo causes mild bone marrow failure and microcephaly. J. Exp. Med. *213*, 1011–1028.

STAR★METHODS

KEY RESOURCES TABLE

REAGENT or RESOURCE	SOURCE	IDENTIFIER
Antibodies		
Rabbit polyclonal anti-RAD51	Bioacademia	Cat#70-001
Mouse anti-HA	Biolegend	Cat#901501; RRID: AB_2565006
Rabbit anti-HA	Cell Signaling	Cat#3724; RRID: AB_1549585
Rabbit anti-SFPQ	Bethyl Laboratories	Cat#A301-321A-M; RRID: AB_2779823
Mouse anti-γH2AX	Millipore	Cat#05-636; RRID: AB_309864
Goat Anti-Mouse IgG (H+L) Highly Cross-Adsorbed Secondary Antibody, Alexa Fluor 488	Thermo Fisher Scientific	Cat# A-11029; RRID: AB_138404
Goat anti-Rabbit IgG (H+L) Highly Cross-Adsorbed Secondary Antibody, Alexa Fluor 488	Thermo Fisher Scientific	Cat# A-11034; RRID: AB_2576217
Goat polyclonal anti-Mouse IgG (H+L) Cross-Adsorbed Secondary Antibody, Texas Red-X	Thermo Fisher Scientific	Cat# T-862; RRID: AB_221654
Goat polyclonal anti-Rabbit IgG (H+L) Cross-Adsorbed Secondary Antibody, Texas Red-X	Thermo Fisher Scientific	Cat#T-6391; RRID: AB_10374713
Biotinylated monoclonal anti-mouse IgA antibody	Thermo Fisher Scientific	Cat# 3-5994-82; RRID: AB_466863
Rabbit polyclonal anti-53BP1	Abcam	Cat#ab21083; RRID: AB_722496
Rabbit Monoclonal anti-RPA32/RPA2 antibody (Clone EPR2877Y)	Abcam	Cat#ab76420; RRID: AB_1524336
Goat polyclonal anti-Rabbit IgG (H+L) Cross-Adsorbed Secondary Antibody, Alexa Fluor 488	Thermo Fisher Scientific	Cat#A-11008; RRID: AB_143165
Goat polyclonal anti-Rat IgG (H+L) Cross-Adsorbed Secondary Antibody, Alexa Fluor 488	Thermo Fisher Scientific	Cat# A-11006; RRID: AB_2534074
Armenian hamster anti-CD40 Monoclonal Antibody (HM40-3), FITC	Thermo Fisher Scientific	Cat# 11-0402-82 ; RRID: AB_465029
Rabbit polyclonal anti-53BP1	Novus Biological	Cat# NB100-304; RRID: AB_10003037
Rabbit polyclonal anti-XRCC4	Abcam	Cat# ab97351; RRID: AB_10679332
Mouse monoclonal anti-MAD2B	BD Bioscience	Cat# 612266; RRID: AB_399583
Rabbit polyclonal anti-Ligase IV	Novus Biological	Cat# NB110-57379; RRID: AB_843838
Mouse monoclonal anti-RIF1	Santa Cruz Biotechnology	Cat# sc-515573
Mouse monoclonal anti- β-Actin	SIGMA	Cat# A2228; RRID: AB_476697
Bacterial and Virus Strains		
Endura Chemically Competent Cells	Lucigen	Cat# 60240-1
ElectroMAX Stbl4 Competent Cells	Thermo Fisher Scientific	Cat#11635018
Chemicals, Peptides, and Recombinant Proteins		
AZD2281 (Olaparib), PARP inhibitor	Syncom, Groningen, the Netherlands	CAS: 763113-22-0
AZD0156, ATM inhibitor	Selleckchem	Cat#S8375
NU7441, DNAPK inhibitor	Selleckchem	Cat#S2638
BMN-673 (Talazoparib), PARP inhibitor	Selleckchem	Cat#S7048; CAS: 1207456-01-6
Recombinant Mouse IL-4 Protein	R&D Systems	Cat#404-ML
Recombinant Mouse TGF-beta 1 Protein	R&D Systems	Cat#7666-MB
BD Phosflow Fix Buffer 1	BD Biosciences	Cat#557870
Critical Commercial Assays		
QIAamp DNAMini Kit	QIAGEN	Cat#51306
MiniElute PCR Purifcation Kit	QIAGEN	Cat#28006
in-fusion HD cloning kit	Takara	Cat#12141

(*Continued on next page*)

Continued

REAGENT or RESOURCE	SOURCE	IDENTIFIER
Duolink proximity Ligation Starter Kit	Sigma	Cat# DUO92101-1KT
Cell titer blue Cell Viability Assay	Promega	G8080
Deposited Data		
TCGA	Broad Institute	https://gdc.cancer.gov/about-data/publications/pancanatlas, http://firebrowse.org, http://www.cbioportal.org/
Experimental Models: Cell Lines		
KB1P-G3	Jaspers et al., 2013	N/A
KB1P-G3B1+	Barazas et al., 2019	N/A
KB2P3.4	Evers et al., 2008	N/A
KB1P4s organoids	Duarte et al., 2018	N/A
HEK293FT	ATCC	RRID:CVCL_6911
KB1P-G3 53BP1 knockout	Barazas et al., 2019	N/A
Brca1$^{-/-}$;Trp53$^{-/-}$mouse embryonic stem cells (mESCs)	Bouwman et al., 2010	N/A
CH12 B cells	Pennell et al., 1985	RRID:CVCL_6818
HAP1	gift from Thijn Brummelkamp, NKI, Amsterdam	N/A
Experimental Models: Organisms/Strains		
Mouse: FU/J Nude mice	Jackson laboratory	N/A
Oligonucleotides		
See Table S6	This paper	
Recombinant DNA		
pGT-EN2	Jae et al., 2013	N/A
pBABE-Neomycin	Addgene	RRID: Addgene_1767
plentiCRISPR v2_Non-targeting sgRNA	This paper	N/A
plentiCRISPR v2_ERCC6L2_sgRNA1	This paper	N/A
plentiCRISPR v2_ERCC6L2_sgRNA2	This paper	N/A
pBABE-Neomycin HA-*Ercc6l2*	This paper	N/A
pBABE-Neomycin HA-*Ercc6l2*$^{\Delta SNF2}$	This paper	N/A
pBABE-Neomycin HA-*Ercc6l2*$^{\Delta Hebo}$	This paper	N/A
pOZ-N-FH-IL2Rα HA	This paper	Dipanjan Chowdhury
pOZ-N-FH-IL2Rα HA-*Ercc6l2*	This paper	N/A
pOZ-N-FH-IL2Rα HA-*Ercc6l2*$^{\Delta SNF2}$	This paper	N/A
pOZ-N-FH-IL2Rα HA-*Ercc6l2*$^{\Delta Hebo}$	This paper	N/A
Software and Algorithms		
STRING	Szklarczyk et al., 2019	Version 11
ImageJ, Fiji, colony area plugin	Bagga et al., 2014; Schindelin et al., 2019; Schneider et al., 2012	ImageJ version 1.50i
CFAssay R package	Braselmann et al., 2015	N/A
TCGAbiolinks	Colaprico et al., 2016	Version 2.14.0
FlowJo	RRID:SCR_008520	Version 10.6.1
GSEA	Subramanian et al., 2005	Version 20.0.3

RESOURCE AVAILABILITY

Lead Contact

Further information and requests for resources and reagents should be directed to and will be fulfilled by the Lead Contact, Sven Rottenberg (sven.rottenberg@vetsuisse.unibe.ch).

Materials Availability

All unique/stable reagents generated in this study will be made available on request, but we may require a payment and/or a completed Materials Transfer Agreement if there is potential for commercial application.

Data and Code Availability

Sequencing of the haploid genetic screens was performed at the Netherlands Cancer Institute. The IR haploid genetic screen results generated during this study are available in Tables S1 and S2. Blomen et al. (2015) includes all the control groups used in the analysis of the screen results.

The UCEC TCGA dataset used in this study is available with informed consent under the authorization of local Institutional Review Boards (https://www.cancer.gov/about-nci/organization/ccg/research/structural-genomics/tcga). Mutation and clinical data (including age and sex) used for this manuscript are deposited by the GDC (https://gdc.cancer.gov/about-data/publications/pancanatlas).

EXPERIMENTAL MODEL AND SUBJECT DETAILS

Mice

All animal experiments were approved by the Animal Ethics Committee of the Netherlands Cancer Institute (Amsterdam, the Netherlands) and the Animal Ethics Committee (BLV Bern, Switzerland, Application number BE40/18). All experiments were performed in accordance with the Dutch Act on Animal Experimentation (November 2014) and the Swiss Act on Animal Experimentation (December 2015). CRISPR-Cas9-modified organoids lines derived from *K14cre; Brca1$^{F/F}$;Trp53$^{F/F}$* (KB1P) female mice were transplanted in 6-9 weeks-old NU/J nude mice for the *in vivo* validation.

Cell Lines

The KB1P-G3 cell line was previously established from a KB1P mouse mammary tumor and cultured as described by Jaspers et al. (2013). The KB1P-G3B1+ cell line was derived from the KB1P-G3 cell line which was reconstituted with human BRCA1 (Barazas et al., 2019). The *Trp53bp1* knockout KB1P-G3 line was generated as described (Barazas et al., 2019). The KB2P-3.4 cell line was previously established from a *K14cre;Brca2$^{F/F}$;Trp53$^{F/F}$* (KB2P) mouse mammary tumor as described (Evers et al., 2008). All these lines were grown in Dulbecco's Modified Eagle Medium/Nutrient Mixture F-12 (DMEM/F12; GIBCO) supplemented with 10% fetal calf serum (FCS, Sigma), 50 units/ml penicillin-streptomycin (GIBCO), 5 μg/ml Insulin (Sigma,#I0516), 5 ng/ml cholera toxin (Sigma, #C8052) and 5 ng/ml murine epidermal growth-factor (EGF, Sigma, #E4127). The HEK293FT cell line (RRID:CVCL_6911) was cultured in Iscove's Modified Dulbecco's Media (IMDM, GIBCO) supplemented with 10% fetal calf serum (FCS, Sigma) and 50 units/ml penicillin-streptomycin (GIBCO). HAP1 cells were a kind gift from Thijn Brummelkamp, NKI, and cultured in IMDM containing 10% fetal bovine serum, 1% penicillin-streptomycin, and 1mM L-glutamine (all reagents from GIBCO). CH12F3 cell lines were cultured in RPMI supplemented with 5% NCTC-109 medium, 10% FCS, 100 U/ml penicillin, 100ng/ml streptomycin and 2mM L-glutamine. Mouse embryonic stem (mES) cells with a selectable conditional *Brca1* deletion (*R26$^{CreERT2/wt}$;Brca1$^{SCo/\Delta}$* and *R26^{CreERT2};Brca1$^{SCo/\Delta}$;Pim1$^{DR\text{-}GFP/wt}$*) (Bouwman et al., 2013) were cultured on gelatin-coated plates in 60% buffalo red liver (BRL) cell conditioned medium supplied with 10% fetal calf serum, 0.1 mM β-mercaptoethanol (Merck) and 10^3 U/ml ESGRO LIF (Millipore).

Tissue culture was carried out under standard conditions (37°C, 5% CO_2), except for KB1P-G3 and KB2P3.4 cells which were cultured under low oxygen conditions (3% O_2). Testing for mycoplasma contamination was performed twice per year.

Tumor-Derived Organoids

The KB1P4 3D tumor organoid line was previously established from a *Brca1$^{-/-}$;p53$^{-/-}$* mouse mammary tumor and cultured as described (Duarte et al., 2018). Briefly, cultures were embedded in Culturex Reduced Growth Factor Basement Membrane Extract Type 2 (BME, Trevigen; 40 μL BME:growth media 1:1 drop in a single well of 24-well plate) and grown in Advanced DMEM/F12 (AdDMEM/F12, GIBCO) supplemented with 1 M HEPES (Sigma), GlutaMAX (GIBCO) 50 U/ml penicillin-streptomycin (GIBCO), B27 (GIBCO), 125 μM N-acetyl-L-cysteine (Sigma) and 50 ng/ml murine epidermal growth factor (Sigma). Organoids were cultured under standard conditions (37°C, 5% CO_2) and regularly tested for mycoplasma contamination.

Further *in vitro* culture details and gene editing details are provided in the Method Details section.

METHOD DETAILS

All details of methodology including statistical analysis are reported in the figures and corresponding figure legends.

Haploid Genetic screens

Wild-type HAP1 cells were mutagenized using a retroviral gene-trap cassette as described previously (Blomen et al., 2015). 10^8 mutagenized HAP1 cells were seeded in 14 T175 cell culture flasks (Corning) with IMDM-Glutmax (GIBCO) media supplemented with 1X Glutmax (GIBCO), 1X penicillin-streptomycin (GIBCO) and 10% FCS (GIBCO). Cells were irradiated after 24h (day 1), 72h

(day 3) and 120h (day5) with 1.5Gy each time which led to a confluency of 70%–80% on day 10. Cells were subsequently dissociated using Trypsin-EDTA, washed with PBS and fixed in pre-warmed BD Phosflow fix buffer I (BD Bioscience) for 10 min at 37°C. Following washing with PBS containing 10% FCS cells were treated with RNase (QIAGEN) (100 μg/ml) for 1h at 37°C, and stained with 10 μg/ml propidium iodide (Life Technologies) before straining through a 40 μm cell strainer (Falcon). At least 30 million cells with 1n DNA content were sorted on a BD Biosciences FACS ARIA III. Genomic DNA was isolated using a QIAmp DNA mini kit (QIAGEN) and Linear Amplification Mediated (LAM)-PCR was performed as described in Blomen et al. (2015) as well as sequencing data processing, insertion site mapping to GRCh38 human genome assembly. The insertion sites were intersected with RefSeq gene coordinates to assign insertions to genes and map their orientation with respect to the transcriptional direction, choosing the longest transcript for each gene and disregarding overlapping regions were orientation assignment is ambiguous. Orientation bias was determined using a binomial test and corrected for false discovery (Benjamini Hochberg). Four independent cultured wild-type control datasets published in the same article were used for normalization (available at SRA SRP058962, accession numbers SRX1045464, SRX1045465, SRX1045466, SRX1045467). The irradiation screens were performed two times with individual mutagenized HAP1 batches. To identify genes that affect cell viability in the presence of IR, for each gene the number of disruptive sense integrations and non-disruptive antisense integrations was compared to that in the four control datasets using a 2-sided Fisher's exact test. Genes with a significant orientation bias after IR treatment in addition to a significantly ($p < 0.05$) altered ratio in relation to the control datasets were considered as hits.

STRING Analysis

Protein interaction map shown in Figure 1E was carried out using the STRING protein-protein interaction network enrichment analysis, version 11.0 with small modifications. Minimum required interaction score was set to 0.4 and the line thickness indicates the strength of data support.

Gene editing, silencing, plasmids, and cloning

Lentiviral transductions

Lentiviral stocks were generated by transient transfection of HEK293FT cells. On day 0, $8x10^6$ HEK293FT cells were seeded in 150cm cell culture dishes and on the next day transiently transfected with lentiviral packaging plasmids and the plentiCRISPRv2 vector containing the respective sgRNA or a non-targeting sgRNA using 2xHBS (280nM NaCl, 100mM HEPES, 1.5mM Na_2HPO_4, pH 7.22), 2.5M $CaCl_2$ and 0.1x TE buffer (10mM Tris pH8.0, 1mM EDTA pH8.0, diluted 1:10 with dH_2O). After 30 h, virus-containing supernatant was concentrated by ultracentrifugation at 20.000rpm for 2h in a SW40 rotor and the virus was finally resuspended in 100 μL PBS. The virus titer was determined using a qPCR Lentivirus Titration Kit (Applied Biological Materials). For lentiviral transduction, 150.000 target cells were seeded in 6-well plates. 24h later, virus at a multiplicity of infection (MOI) of 25 was applied with 8 μg/ml Polybrene (Merck Millipore). Virus-containing medium was replaced with medium containing puromycin (3.5 μg/ml, GIBCO) 24h later. Puromycin selection was performed for three days; subsequently cells were expanded and frozen down at early passage. Tumor-derived organoids were transduced according to a previously established protocol (Duarte et al., 2018). The target sites modifications of the polyclonal cell pools were analyzed by TIDE analysis which is described below.

Genome editing

Generation of CRISPR/Cas9 plasmids, unless otherwise stated, were performed using a modified version of the lentiCRISPR v2 backbone (RRID: Addgene_52961) in which a puromycin resistance ORF was cloned under the hPGK promoter. sgRNA sequences were cloned in the lentiCRISPR v2 backbone using custom DNA oligos (Microsynth) which were melted at 95°C for 5 min, annealed at RT for 2 h and subsequently ligated with quick-ligase (NEB) into BsmBI-digested (Fermantas) backbone. All constructs sequences were verified by Sanger sequencing. sgRNA sequences are provided below as well as in Table S7.

ERCC6L2 reconstitution was performed using the pBABE-neomycin (RRID: Addgene_1767) plasmid or pOZ-N-FH (kindly provided by Dipanjan Chowdhury, Harvard Medical School). The *Ercc6l2* coding sequence was ordered from Eurofins with optimized modifications for *Mus musculus.* The coding sequence was cloned into pBABE-neomycin adding 1x HA tag at the N terminus using the in-fusion HD cloning kit (#12141, Takara) (see Key Resources Table) or into pOZ-N-FH. Fulllength wild-type *Ercc6l2* coding sequence was mutated in the following sites: SNF2 mutant (*Ercc6l2*$^{\Delta SNF2}$): c.1796A>G, Hebo mutant (*Ercc6l2*$^{\Delta Hebo}$): c.4696T>G, c.4699T>G.

Rev7$^{-/-}$and *Ercc6l2*$^{-/-}$ CH12-F3 were generated using CRISPR–Cas9. In brief, gene-specific sgRNAs (sequences below) were cloned in modified pX330 (Addgene #42230) or pX458 vectors (Addgene #48138). CH12-F3 cells were nucleofected (Amaxa Nucleofector 2b, Lonza) with 2 μg of plasmid and Cell Line Nucleofector Kit R (Lonza), using program D-023. Isogenic cell clones were isolated by limiting dilution (pX330) or GFP sorting (pX458) single cell into 96-well plates. Clones bearing bi-allelic indel mutations were identified by native PAGE resolution of PCR amplicons corresponding to edited loci (amplicon primer sequences below), and gene disruption subsequently confirmed by Sanger sequencing.

Rev7 sgRNA: 5′-CCTGATTCTCTATGTGCGCG-3′ targeting exon 1
Ercc6l2 sgRNA1: 5′-TGAAACACTGCGCTTGTGTC-3′ targeting exon 2
Ercc6l2 sgRNA3: 5′-GGAAGGATGAATTGGATACC-3′ targeting exon 2
Amplicon primers for *Rev7* and *Ercc6l2* are provided in Table S7.

Complemented CH12-F3 cell lines were generated by lentivirus-mediated transduction, using viral supernatants collected from 293T cells co-transfected with third generation packaging vectors and pLenti-PGK-Flag-HA-PURO-DEST vectors containing cloned transgene inserts. Typically, cells were spinoculated with polybrene (8 μg/ml) and HEPES (20mM)-supplemented viral supernatants (1500 rpm, 90 min at 25°C). Stable cell-lines were subsequently selected and maintained in the presence of puromycin (1 μg/ml).

gDNA isolation, amplification, and TIDE analysis

To assess modification rate, cells were pelleted and genomic DNA was extracted using the QIAmp DNA mini kit (QIAGEN) according to manufacturer's protocol. Target loci were amplified using Phusion High Fidelity Polymerase (Thermo Scientific) using a 3-step protocol: (1) 98°C for 30 s, (2) 30 cycles at 98°C for 10 s, 63.8°C for 20 s and 72°C for 30 s, (3) 72°C for 5min. Reaction mix consisted of 10ul of 2X Phusion Mastermix (Thermo Fisher), 1ul of 20uM forward and reverse primer and 100ng of DNA in 20ul total volume. PCR products were purified using the QIAquick PCR purification kit (QIAGEN) according to manufacturer's protocol and submitted with corresponding forward primers for Sanger sequencing to confirm target modifications using the TIDE algorithm (Brinkman et al., 2014). Primers used in this PCR are mentioned in Table S7.

CRISPR sgRNA sequences for modification of *Ercc6l2* were chosen from the GeCKo library v2 (Sanjana et al., 2014). The sgRNA sequences are provided in Table S7.

Clonogenic assays

To assess their clonogenic potential, KB1P-G3B1+ or KB1P-G3 cells were seeded in 10cm dishes (1000 cells/dish) and treated with the indicated dose of IR 24 h later. IR-treated cells were exposed to single dose of IR. All the dishes were fixed 10 days after seeding with 4% formalin and stained with 0.1% crystal violet. Colonies were counted with ImageJ using macros in an automated manner.

Growth assays

For growth assays in 6 wells format, 2000 KB1P-G3B1+ or 4000 KB1P-G3 cells were seeded per well and treated with the mentioned drug or irradiation at the indicated dosages after 24 h. IR-treated cells were subsequently exposed to repeated irradiation on day 2 and 3. Olaparib treated cells were constantly exposed to olaparib during the course of the experiments. Control wells were fixed with 4% formalin and stained with 0.1% crystal violet on day 8, whereas treated cells were fixed and stained on day 11, and cells for TIDE analysis were collected on the corresponding days. Quantification of plates was performed with ImageJ using macros in an automated manner.

For growth assays in 96 wells format, 150 KB1P-G3B1+ cells were seeded per well and treated with the indicated siRNAs two times on day 1 and day 2. siRNA were transfected using Lipofectamine RNAiMAX (Thermo Fisher) following manufacturer's instructions. On day 3, cells were treated with IR at the indicated dosages. Proliferation was measured on day 10 using the CellTiter-Blue® Cell Viability Assay (Promega) following manufacturer's instructions.

Western blotting

Cells were washed with PBS, lysed in RIPA buffer (50 mM Tris/HCl pH 7.4; 1% NP-40; 0.5% Na-deoxycholate; 0.1% SDS; 150 mM NaCl, 2 nM EDTA, 50 mM NaF) containing complete protease inhibitor cocktail (Roche) for 30 min on ice, and cleared by centrifugation. Protein concentration was determined using Pierce BCA assay kit (Thermo Fisher Scientific) with a BSA standard curve. Before loading, protein lysates were denatured at 95°C for 5 min in 6x SDS sample buffer. Proteins were separated by SDS/ PAGE on 7.5 or 12% gels before semi-dry transfer to 0.45 lm nitrocellulose membranes (GE Healthcare) and blocked in 5% dry milk powder in TBS-T (100 mM Tris, pH 7.5, 0.9% NaCl, 0.05% Tween-20). Membranes were incubated with primary antibodies diluted in 5% BSA in TBS-T at 4°C over night. After washing in TBS-T, Horseradish Peroxidase (*HRP*)-linked secondary antibodies (Cell Signaling, dilution 1: 2500) were applied for 1 h at room temperature. Images were acquired using Azure c600 chemiluminescent imager.

In vivo studies

For tumor organoid transplantation: organoids were collected, incubated with TripLE at 37°C for 5min, dissociated into single cells, washed in PBS, resuspended in tumor organoid medium and mixed in a 1:1 ratio of tumor organoid suspension and BME in a cell concentration of 10^4 cells per 40 μl. Subsequently, 10^4 cells were transplanted in the fourth right mammary fat pad of 6-9 week-old NMRI nude mice. For tumor piece transplantation, DMSO-frozen tumor pieces were thawed, washed with PBS, cut into small pieces and transplanted in the fourth right mammary fat pad of 6-9 week-old NMRI nude mice. Mammary tumor size was measured by caliper and tumor volume was calculated (length x width^2 /2). Treatment of tumor bearing mice was initiated when tumors reached a size of ~150mm^3, at which point mice were separated into two untreated/vehicle groups (n = 4x2), olaparib treatment group (n = 5-7/sgRNA) or radiotherapy treated group (n = 5-7/sgRNA). Olaparib was administered at 100 mg/kg intraperitoneally for 56 consecutive days. Radiotherapy was delivered using a high-precision small-animal irradiator equipped with a cone-beam CT scanner (X-RAD 225Cx). The dosing schedule consisted of 24Gy/4fr in 2 weeks. Animals were anesthetized with isoflurane, sacrificed with CO_2 followed by cervical dislocation when the tumor reached a volume of 1500mm^3.

Immunoflorescence staining and RAD51 irradiation induced foci (IRIF) analysis

RAD51 immunofluorescence in CRISPR/Cas9-modified KB1P-G3 and KB1P-G3B1+ cells was performed as described previously (Xu et al., 2015), with minor modifications.

Cells were grown on coverslips in 24-well plates. IRIF were induced by γ-irradiation (10Gy) 3 h prior to fixation. Subsequently, cells were washed in PBS and fixed with 4% PFA/PBS for 20min on ice. Fixed cells were washed with PBS and permeabilized for 20min in 0.2% Triton X-100/PBS. All subsequent steps were performed in staining buffer (PBS, BSA (2%), glycine (0.15%), Triton X-100 (0.1%)). Cells were washed 3 times and blocked for 30min at RT, incubated with the primary antibody for 1 h at RT (rabbit-anti-RAD51 (70-001, BioAcademia,1:1000), mouse-anti-HA (RRID: AB_2565006, 901501, Biolegend, 1:800), rabbit-anti-HA (RRID:AB_1549585, #3724, CST, 1:800), rabbit-anti-SFPQ(RRID:AB_2779823, A301-321A-M, Bethyl Laboratories, 1:250), mouse-anti- γH2AX (RRID:AB_309864, 05-636, Millipore, 1:500)), washed 3 times, incubated with the secondary antibody for 1 h at RT (Texas Red- goat anti-rabbit IgG (RRID: AB_10374713, T6391, Thermo Fisher Scientific, 1:2500), Texas Red goat anti-mouse IgG (RRID:AB_221654, T862, Thermo Fisher Scientific,1:2500), Alexa Fluor 488 goat anti-mouse IgG (RRID: AB_138404, A11029, Thermo Fisher Scientific,1:2500), Alexa Fluor 488 goat anti-rabbit IgG (RRID: AB_2576217, A11034, Thermo Fisher Scientific,1:2500),), washed 3 times, counterstained with DAPI (Life Technologies, 1:50000 dilution) and washed 5 times more before mounting. Antibodies were diluted in staining buffer. Last, cells were mounted using fluorescence mounting medium (S3023, Dako). Fluorescent images were acquired using a Delta Vision widefield microscope (GE Healthcare Life Sciences) and multiple different fields were imaged per sample (60x objective). Images were analyzed and foci quantification analysis was performed using FIJI image processing package of ImageJ (1.8.0). Briefly, all nuclei were detected by the ''analyze particles'' command and all the RAD51 foci per nucleus were counted with the ''finding maxima'' command. Data were plotted and the significance was calculated using 2-way ANOVA followed by Dunnett's multiple comparisons test. *$p < 0.05$, **$p < 0.01$, ***$p < 0.001$.

Proximity ligation assay (PLA)

Proximity ligation assay (DUO92101-1KT, Sigma) was used to show the interaction between HA-ERCC6L2 (RRID: AB_2565006, 901501, Biolegend, 1:800) and endogenous SFPQ (RRID: AB_2779823, A301-321A-M, Bethyl Laboratories, 1:250) according to the manufacturer's protocol. Cells were grown on coverslips in 24-well plates. IRIF were induced by γ-irradiation (10Gy) 3 h prior to fixation. Subsequently, cells were washed in PBS and fixed with 4% PFA/PBS for 20min on ice. Fixed cells were washed with PBS and permeabilized for 20min in 0.2% Triton X-100/PBS. All subsequent steps were performed in staining buffer (PBS, BSA (2%), glycine (0.15%), Triton X-100 (0.1%)). Cells were washed 3 times and blocked for 1.5hours at RT, incubated with the indicated primary antibody for 2 h at RT. PLA probe mix was prepared according to the recommended dilution and 40ul/slide was added after slides were washed with 6mlx2 staining buffer, Cells were then incubated in humidity chamber for 1 h at 27°C. Ligation and amplification steps were followed according to the manufacturer's recommendations and wash buffers. Slides were fixed with 3ul/slide of Duolink *In Situ* Mounting Medium (included in the starter kit). Fluorescent images were acquired using a Delta Vision widefield microscope (GE Healthcare Life Sciences) and multiple different fields were imaged per sample (60x objective). Images were analyzed and foci quantification analysis was performed using FIJI image processing package of ImageJ (1.8.0).

DR-GFP Assay

mES cells were cultured as described (Bouwman et al., 2013). To allow analysis of homology-dependent DNA double strand break repair, the Pim1 locus of $R26^{CreERT2/wt}$;$Brca1^{SCo/\Delta}$ mouse ES cells was targeted with the p31kDR-GFP plasmid (Reid et al., 2008). $R26^{CreERT2/wt}$; $Brca1^{SCo/\Delta}$; $Pim1^{DR\text{-}GFP/wt}$. mES cells were transduced overnight with *sgErcc6l2* and *sgNT* lentiCRISPRv2 virus at an MOI of 10 in the presence of 8 μg/ml and stable integration was selected using 1.8 μg/ml puromycin. DR-GFP assays were performed essentially as described (Bouwman et al., 2013). In brief, mouse *Brca1* was switched off using a 1 day incubation with 0.5 μM 4-OHT, cells were cultured for 3 days and seeded for Lipofectamine 2000 transfections with I-SceI-mCherry on the next day. Two days after transfection, mCherry/GFP double-positive cells were monitored by flow cytometry on an LSRFortessa (BD Biosciences) cell analyzer and data were analyzed using FlowJo software (FlowJo LLC, BD Biosciences).

RPA loading assay

Laser microirradiation was performed as described previously (Eid et al., 2010). Briefly, 10 μM BrdU was added to cells 24h prior to irradiation. Microirradiation was performed using a MMI CELLCUT system containing a UV A laser of 355 nm (Molecular Machines and Industries, Zurich, Switzerland). The laser intensity was set to 50% energy output and each cells was exposed to the laser beam for < 300ms. After a release of 2h cells were fixed in 4% formaldehyde (w/v) in PBS for 15 min and permeabilized with Triton X-100 (0.5% in PBS) for 5 min at room temperature. Subsequently, cells were blocked for 1h in 3% FCS (w/v) in PBS and stained with primary antibodies 53BP1 (abcam, ab21083, RRID:AB_722496, rabbit, 1:500) and RPA (EPR2877Y, abcam, ab76420, RRID:AB_1524336, rat, 1:100). After staining with appropriate secondary antibodies Alexa Fluor-488 rabbit and Alexa Fluor-594 rat (1:1000) (Life Technologies), coverslips were mounted with Vectashield (Vector Laboratories) containing DAPI and sealed. Images were acquired on a Leica DMI6000. RPA co-localization with 53BP1 was analyzed by fluorescence microscopy.

CSR Assay

Immunoglobulin CSR was performed as described previously (Xu et al., 2015). Briefly, to promote CSR to IgA, CH12-F3 cells were stimulated with agonist anti-CD40 antibody (0.5 μg/ml; Miltenyi Biotec; FGK45.5), mouse IL-4 (5ng/μl; R&D Systems) and TGFβ1 (2. ng/μl; R&D Systems). Cell-surface IgA expression was determined by flow cytometric staining with anti-mouse IgA-FITC antibody (Thermo Fisher; 11-4204-82; MA-6E1).

CH12-F3 proliferation assay

CH12-F3 proliferation was monitored by dye dilution using carboxyfluorescein succinimidyl ester (CFSE) according to manufacturer's instructions (CellTrace; Life Technologies). Cells were labeled with CFSE immediately before cytokine stimulation, and cell proliferation was assessed by flow cytometry at indicated time points.

Immunoprecipitation

500μg of protein lysates were incubated overnight at 4°C with 50μl of Dynabeads Protein G magnetic beads (Invitrogen), previously coupled to 5 μg of pull-down antibody. Beads were washed 3 times by gentle pipetting with 0.02% Tween 20 and eluted by boiling in 2x sample buffer for 10'. Pull-downs and whole cell extracts were loaded onto SDS/PAGE gels, followed by immunoblotting and probing with indicated antibodies.

Yeast two–hybrid screen

Yeast two-hybrid (Y2H) screen was performed as a service by Hybrigenics S.A. (Paris, France). More than 51 million interactions were tested using a mouse inner ear cDNA library and a C-terminal region of ERCC6L2 (aa 885-1360) as bait. The 1-by-1 validation of ERCC6L2 and SFPQ was also performed by Hybrigenics S.A. (Paris, France) as previously described (Alhamidi et al., 2011).

TCGA data analysis

To verify the clinical impact of *ERCC6L2* mutations and *ERCC6L2* expression level in human cancers, we used the data generated by The Cancer Genome Atlas (TCGA) consortium. TCGA is a cancer genomics program that collected and molecularly characterized >20,000 matched tumor and normal samples representing 33 cancer types, with informed consent under the authorization of local Institutional Review Boards (https://www.cancer.gov/about-nci/organization/ccg/research/structural-genomics/tcga). Mutation and clinical data (including age and sex) used for this manuscript are deposited by the GDC (https://gdc.cancer.gov/about-data/publications/pancanatlas).

Data acquisition and preparation

We decided to restrict our analyses of clinical impact of *ERCC6L2* mutations to the UCEC cohort in TCGA because it was the cohort harboring the highest number of such mutations (Figure 6A). The variables histological_type, histological_grade, OS, OS.time, DSS and DSS.time were obtained from a recent paper integrating pan-cancer clinical data for all TCGA cohorts in a standardized manner (Liu et al., 2018).Treatment data related to RT were extracted from clinical files from Firebrowse (Broad institute, http://firebrowse.org) on 17 Oct 2019. Mutation data and mRNA expression data that were used in this study were generated by the TCGA Research Network, are made available through the NCI Genomic Data Commons and cBioPortal (http://www.cbioportal.org/) and were downloaded on 17 Oct 2019. The detailed mutation information for all patients in the TCGA UCEC cohort, as downloaded from cBioPortal, is presented in Table S6. mRNA expression data for cancer and normal tissue comparison in the TCGA UCEC cohort were downloaded from the Synapse TCGA_PanCancer repository (synapse accession: syn300013).

Scores for telomeric-allelic imbalance (TAI), large-scale transition (LST), loss-of-heterozygosity (HRD LOH) and Homologous Recombination Deficiency (HRD) were derived as described in Knijnenburg et al. (2018). TAI represents the number of subchromosomal regions with allelic imbalance extending to the telomere, LST is the number of chromosomal breaks between adjacent regions of at least 10Mb, HRD LOH is the number of loss-of-heterozygosity regions of intermediate size (< 15Mb but < whole chromosome in length) and HRD Score is calculated from the three scores (TAI + LST + HRD LOH). Survival and clinical data, information about treatment with RT, *ERCC6L2* mutation, expression, and copy-number alterations, as well as HRD scores were compiled into a single matrix (Table S5).

HRD Score and ERCC6L2 mRNA expression correlation in samples from the TCGA UCEC cohort

We tested for correlations between the HRD Score and its components and *ERCC6L2* mRNA expression using Spearman's rank correlation test and reported Spearman's rank coefficients and *p* values.

Comparison of the ERCC6L2 mRNA expression between solid tumor and normal samples from the TCGA UCEC cohort

Samples were grouped based on the material type: solid tumor or solid tissue normal. Furthermore, tumor and normal tissue paired patients of the UCEC cohort were plotted on Figure S6.

Comparison of HRD Score and its constituents between ERCC6L2mut and ERCC6L2wt samples

We compared the DNA damage response (DDR) footprints, including HRD Score and its constituents, between *ERCC6L2* mutant and *ERCC6L2* wild-type samples with Mann-Whitney's U test. Other scores defined in (Knijnenburg et al., 2018) are calculated for *ERCC6L2* mutant and *ERCC6L2* wild-type groups (Table S5).

Assessment of the clinical impact of ERCC6L2 mutations on the overall and disease-specific survival in TCGA UCEC patients—univariate analysis

We analyzed the impact of *ERCC6L2* mutations presence on overall survival (OS) of the patients from TCGA UCEC cohort who received radiotherapy. Hazard ratios (HR), 95% confidence intervals and *p* values are reported for this analysis (Figure 6F).

Gene set enrichment analysis

We performed Gene Set Enrichment Analysis on *ERCC6L2* mutant (n = 43) versus *ERCC6L2* wild-type (n = 470) samples from the TCGA UCEC cohort using GSEA module (v20.0.3) on GenePattern Cloud. Gene expression profiles for all UCEC samples were downloaded using TCGAbiolinks R package. HTSeq-FPKM values were used. Samples were annotated as *ERCC6L2* mutant or *ERCC6L2* wild-type using mutation data downloaded from cbioportal. All GSEA settings were used as default (number of permutations to perform: 1000, permutation type: phenotype, collapse dataset = True, metric for ranking genes: Signal2Noise, scoring scheme: weighted, gene list sorting mode: real, gene list ordering mode: descending, max gene set size: 500, min gene set size: 15).

QUANTIFICATION AND STATISTICAL ANALYSIS

All information regarding statistical analysis including sample size, applied statistical tests and significance are reported in the figures and corresponding figure legends.

Haploid Genetic screens

See Figures 1B, 1C, S1A, and S1B. Analysis was performed as previously described (Blomen et al., 2015). The identified candidates were required to pass a FDR-corrected binominal test with $p < 0.05$, a FDR-corrected Fisher's exact test with $p < 0.05$ comparing the IR screens with the four wild-type control screens, and had to be either depleted or enriched for sense integrations in both replicates. In Figures 1B and 1C, significant hits in comparison to four individual controls screens were shown in red.

Clonogenic Assays

See Figures 2F, 3B, 5A, 5D, and S2N. All experiments indicated in these figures were performed as least three individual biological replicates and graphs were drawn from these data using GraphPad prism 7. Each condition was normalized to the corresponding untreated control. Clonogenic survival capacity data were fitted to the linear quadratic model and statistical analysis was performed using the CFAssay package in R Bioconductor (version 3.4.2)

Growth Assays

See Figures 2H, 3D, S2P, and S2Q. All experiments indicated in these figures were performed as at least three individual biological replicates and graphs were drawn from these data using GraphPad prism 7. Each condition was normalized to the corresponding untreated control. Inhibition cell growth was fitted to four parameter logistic (4PL) sigmoidal curve where concentration of the drug was plotted on the x axis in logarithmic scale. Statistical analysis was performed using 2-way ANOVA followed by Dunnett's test in Graphpad prism 7.

In Figures 4D, 4F, S2C, S2E, S2G, S2I, S2K, and S2M each condition is normalized to the corresponding untreated control and plotted in bar graphs using GraphPad prism 7. Statistical analysis was performed using 2-way ANOVA followed by Dunnett's test in GraphPad prism 7.

In vivo studies

See Figures 3F and 3G. 4 mice were used in each control (untreated or vehicle treated) group in both of the Figures. 5-6 mice were used in each treatment condition. Kaplan Meyer survival curves were plotted and statistical analysis was performed using log-rank test in GraphPad prism 7.

RAD51 IRIF analysis

See Figures 4A, 4B, S4A, S4B, S4D, and S4E. Each condition was stained as indicated in the Method Details section. 60x (with oil) images were taken with a GE Deltavision fluorescent microscope. Each image was taken in 6 Z-layers and Z axis was projected into one layer for quantification. Each nucleus was defined as a particle by thresholding. The amount of RAD51 foci per cell was quantified by finding maxima in each defined particle. At least 300 cells were quantified from each condition and the number of foci per cell was plotted. The experiment was repeated at least three times and one representative biological replicate is shown. Statistical difference of quantification of RAD51 foci between the irradiated (red) samples were analyzed by nonparametric Mann-Whitney test.

DR-GFP Assay

See Figures 4C and S4C. HR activity was determined by flow cytometry and was calculated as the percentage of GFP+ cells in the mCherry+ population relative to BRCA1-proficient parental cells. The amount GFP/mCherry positive cells was counted using FACS and the percentage data were plotted using GraphPad prism 7. The experiment was performed three times and the error bars indicate the standard deviation between three independent transfections. Statistical significance was calculated using the two-tailed Student's t test. * $p < 0.05$, ** $p < 0.01$, ***$p < 0.001$.

CSR Assay

See Figures 5B, 5C, S5B, and S5C. IgA positive cells were counted using FACS and two-three biological replicates were plotted using GraphPad prism 7. Statistical analysis was performed using one-way ANOVA followed by Tukey's multiple comparison test. *$p < 0.05$, **$p < 0.01$, ***$p < 0.001$.

RPA loading assay

See Figure 4H. RPA/53BP1 double positive laser tracks were scored and normalized to the total number of 53BP1 positive tracks. At least 100 cells were analyzed per condition. The experiment was performed four times, and in each independent experiment, a minimum of 100 tracks were analyzed. Data are plotted as mean ± SD. Significance was calculated by one-way ANOVA followed by Tukey's multiple comparison test. *$p < 0.05$, **$p < 0.01$.

TCGA data analysis

See Figures 6B, 6C, 6D, and 6F. Comparison of *ERCC6L2* expression between normal and tumor groups in Figure 6B and difference in HRD score between *ERCC6L2* wild-type and mutant patients (Figure 6C) were shown by using the Mann-Whitney U test. Goodness of fit to the linear regression with 95% confidence interval was demonstrated with the R value as well as *p* value in Figure 6D. Overall survival of patients harboring *ERCC6L2* mutations was compared to *ERCC6L2* wild-type patients via Kaplan Meyer curve and the statistical analysis was performed using log-rank test (Figure 6F). *$p < 0.05$, **$p < 0.01$, ***$p < 0.001$.